POLITECNICO
MILANO 1863

SCUOLA DI INGEGNERIA INDUSTRIALE
E DELL'INFORMAZIONE

Growth and Characterization of $YBa_2[Cu_{0.95}Zn_{0.05}]_3O_{7-\delta}$ Thin Films

Tesi di Laurea Magistrale in
Nuclear Engineering-Ingegneria Nucleare

Author: **Luis Enrique Cueva Guzman**

Student ID: 225544
Advisor: Prof. Giacomo Ghiringhelli
Co-advisors: Prof. Riccardo Arpaia
Academic Year: 2024-25

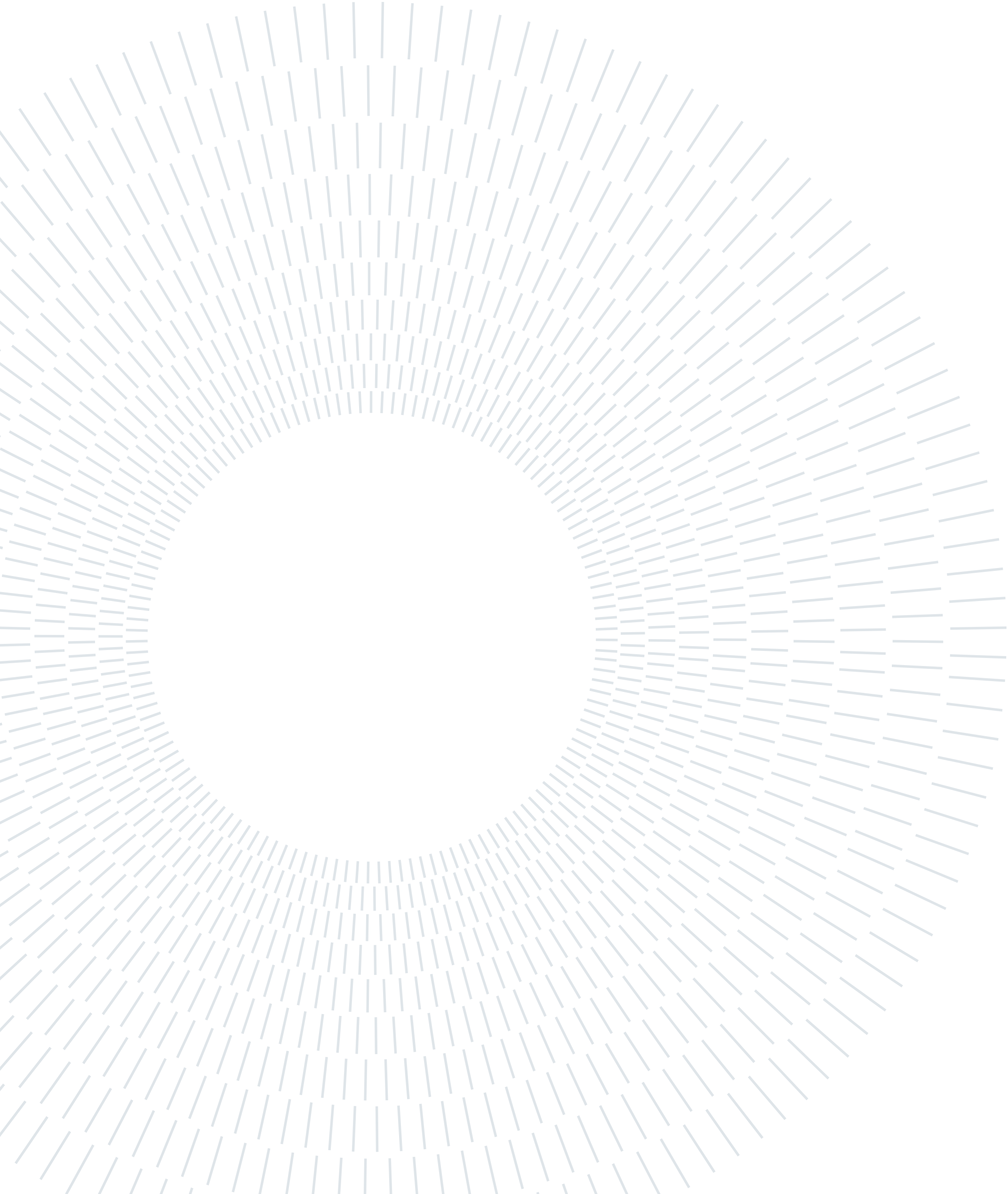

Abstract

The goal of this thesis was to grow, by Pulsed Laser Deposition (PLD), thin films of the cuprate high-critical temperature superconductor $YBa_2[Cu_{0.95}Zn_{0.05}]_3O_{7-\delta}$ (Zn-YBCO). Here, a chemical doping, provided by the replacement of a tiny amount of Cu atoms with Zn, is done in order to significantly reduce the superconducting critical temperature of $YBa_2Cu_3O_{7-\delta}$ (YBCO) modifying in a negligible way the crystal structure and ground state. At the first stage, the primary purpose was to determine the optimal growth parameters. The optimization of the films was carried out using the aid of X-ray diffraction (XRD) to assess the crystalline quality of the films. At a second stage, once optimized films have been achieved, the depositions were performed at different post-annealing oxygen pressures so as to span a broad doping range. Here, temperature-dependent resistivity measurements were performed in order to determine, in combination with lattice parameter data obtained via XRD, the doping levels of the Zn-doped YBCO thin films. Based on this analysis, I constructed the phase diagram of Zn-doped YBCO and compared it with that of pristine YBCO. This comparison allowed me to highlight both similarities and differences between the two systems, with a focus on both the superconducting and normal-state properties. The development of this new material platform—where superconductivity is systematically suppressed through chemical doping—opens the way to a more comprehensive investigation of the symmetry-breaking orders that characterize the normal state of cuprate high-T_c superconductors and compete with superconductivity, such as charge density waves and their associated fluctuations. In particular, the suppression of the superconducting phase allows these competing orders to be explored over a much broader temperature range, extending to low temperatures. This thesis lays the groundwork for a wide range of future experiments, both in transport and spectroscopy, aimed at identifying the fundamental interactions responsible for the emergence of the unconventional ground state in cuprates.

Keywords: Thin Films of Superconductors; Zn-doped YBCO; X-ray Diffraction (XRD); Phase Diagram; Transport Properties.

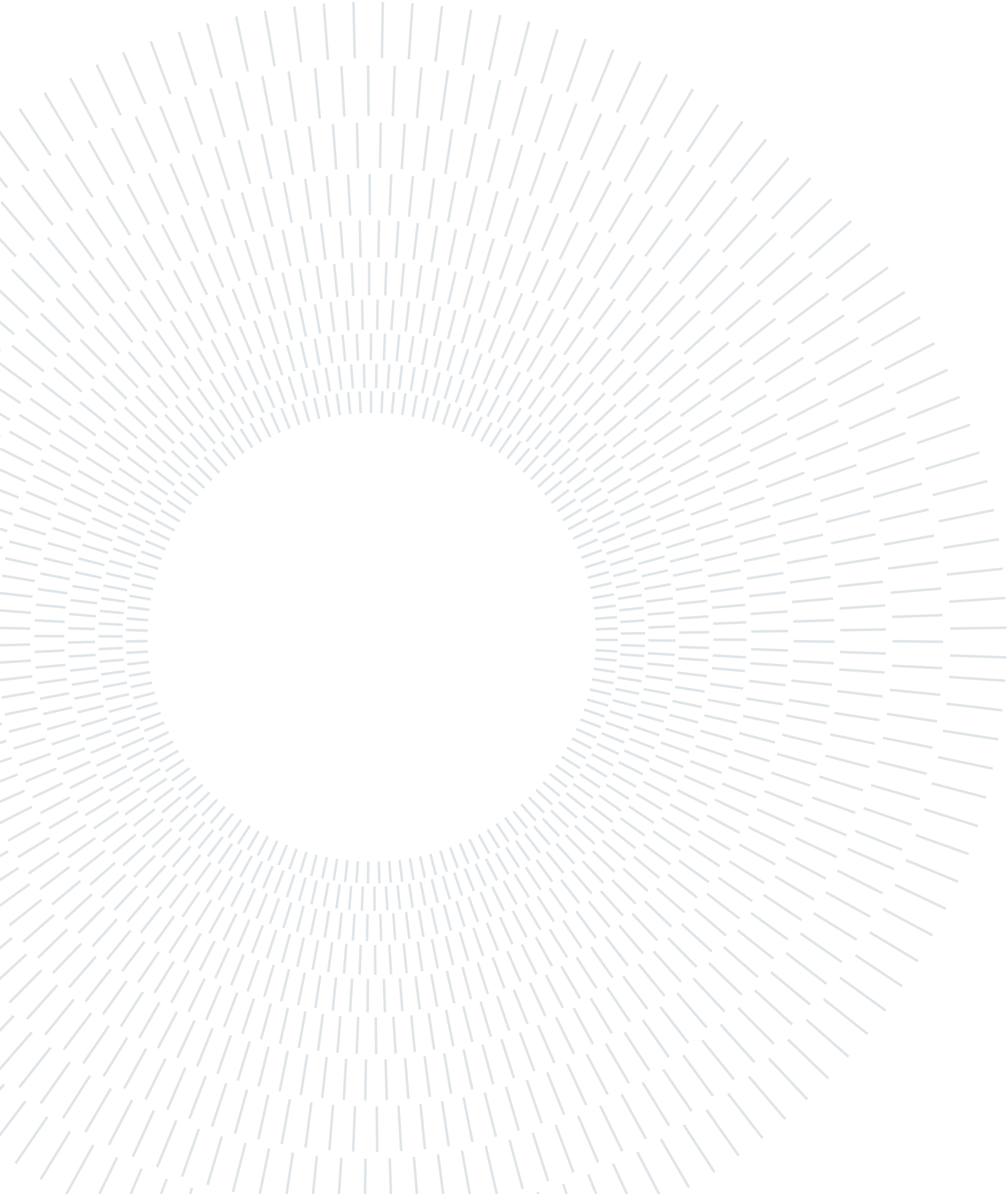

Abstract in lingua italiana

L'obiettivo di questa tesi è stato far crescere, mediante Pulsed Laser Deposition (PLD), film sottili del superconduttore cuprato ad alta temperatura critica $YBa_2[Cu_{0.95}Zn_{0.05}]_3O_{7-\delta}$ (Zn-YBCO). Qui, un drogaggio chimico, ottenuto sostituendo una piccola quantità di atomi di Cu con Zn, è stato effettuato allo scopo di ridurre significativamente la temperatura critica superconduttiva di $YBa_2Cu_3O_{7-\delta}$ (YBCO) modificando in modo trascurabile la struttura cristallina e lo stato fondamentale. In una prima fase, lo scopo principale è stato determinare i parametri di crescita ottimali. L'ottimizzazione dei film è stata effettuata con l'ausilio della diffrazione ai raggi X (XRD) per valutare la qualità cristallina dei film. In una seconda fase, una volta ottenuti film ottimizzati, le deposizioni sono state eseguite a diverse pressioni di ossigeno nel post-annealing, in modo da coprire un ampio intervallo di drogaggio. Sono state quindi effettuate misure di resistività in funzione della temperatura per determinare, in combinazione con i dati dei parametri reticolari ottenuti tramite XRD, i livelli di drogaggio dei film sottili di YBCO drogati con Zn. Sulla base di questa analisi, ho costruito il diagramma di fase dello YBCO drogato con Zn e l'ho confrontato con quello dello YBCO puro. Questo confronto mi ha permesso di mettere in evidenza sia le somiglianze sia le differenze tra i due sistemi, con un'attenzione sia alle proprietà superconduttive sia a quelle dello stato normale. Lo sviluppo di questa nuova piattaforma di materiali — in cui la superconduttività è sistematicamente soppressa tramite drogaggio chimico — apre la strada a un'indagine più completa degli ordini di rottura di simmetria che caratterizzano lo stato normale dei superconduttori cuprati ad alto T_c e competono con la superconduttività, come le onde di densità di carica e le relative fluttuazioni. In particolare, la soppressione della fase superconduttiva consente di esplorare questi ordini concorrenti su un intervallo di temperatura molto più ampio, estendendosi fino alle basse temperature. Questa tesi getta le basi per un'ampia gamma di esperimenti futuri, sia di trasporto sia di spettroscopia, volti a identificare le interazioni fondamentali responsabili dell'emergere dello stato fondamentale non convenzionale nei cuprati.

Parole chiave: Film Sottili di Superconduttori; YBCO drogato con Zn; XRD; Diagramma di Fase; Proprietà di Trasporto.

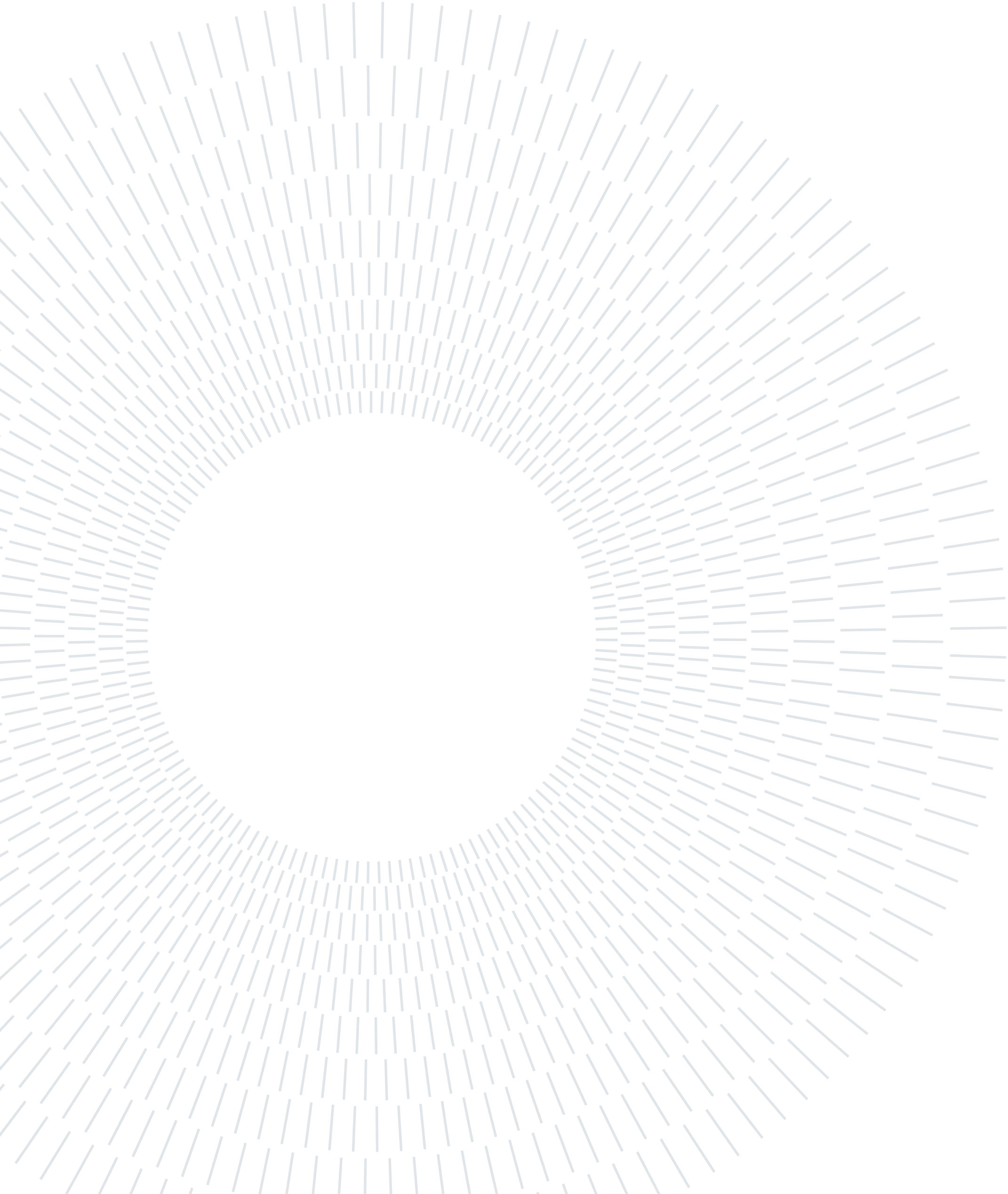

Acknowledgements

I would like to begin by thanking Prof. Ghiringhelli, who gave me the opportunity to carry out my thesis at Chalmers University of Technology, and Prof. Riccardo Arpaia, who was my supervisor in Gothenburg—not only for his patience and dedication in helping me complete my work, but also because he proved to be a truly remarkable person: very kind, always available, and with a passion for his work that I have rarely seen in my life. I apologize for taking a bit longer to complete this thesis; unfortunately, some obstacles caused delays.

If I have reached this point in my academic career, it is mainly thanks to the support of my family, and I would like to thank each of them personally. To my mother, the kindest person in the world: your willingness to help others has always amazed me; I have always admired your strength of will and how, after arriving in a country where you knew practically no one and facing countless difficulties and harsh situations, you remained the same good person. If one day I manage to be even one percent of the person you are, I will consider myself fortunate. To my stepfather Claudio, who never hesitated to help us, was always with us when we needed him, and introduced us to Italian culture when we arrived. To my sister Helen, who has been more than a sister—a second mother—someone I could always rely on, whose strong character and ability to stand up for herself I have always admired; I have been lucky to have you in my life.

I also thank my friends in Genoa—Ascia, Fratino, Andy, Marifer—and the many new people I have met since arriving in Genoa, as well as some more recently during this last period after returning (ESN). Thank you for supporting and putting up with me all this time: with you I have shared many laughs, drunken nights, “insults,” and even a quarantine that seemed about to destroy the world; you have been great companions over these years.

More generally, I want to thank the people who made my time in Milan better (even though, between Covid and an overseas thesis, I wasn’t there very much XD): people like Gabriel, Antonio, Francesco, Jessica, and others I met along the way. Even if we no longer see each other in person, know that you made gray Milan more pleasant and colorful.

Last but not least, I would like to thank the people who accompanied me during my time in Gothenburg: Noemi, Giada, Esther, and many others I met during that period. Every time I think of those days, thanks to you I feel a bit nostalgic for a place so far away, but which was home for a while.

Before closing this section, I just want to say that I will surely forget to thank someone who was fundamentally helpful along the way, and I apologize for that: in these last years, whenever I felt lost and desolate, there was always someone who—even if only for a brief period in my life—helped me get back on my feet. To all of you, I must say thank you: even if it seemed like a small gesture to you, you have no idea how much you have changed my life.

Contents

1 | Key Concepts of Superconductivity

1.1. Discovery and properties of Superconductors

Superconductors are materials that could potentially revolutionize the society we live in due to their zero electrical resistance and perfect diamagnetism. These phenomena occur below a certain critical temperature, which is why they were first discovered by physicist Kamerlingh Onnes in 1911 [1], who observed that the resistance of mercury immersed in liquid helium vanished at $T_c = 4.2$ K. Onnes realized that mercury had transitioned to a new state of matter, which came to be defined as the superconducting state. Later, in 1933, Walther Meissner and Robert Ochsenfeld, while studying the magnetic flux in samples of tin and lead cooled below their critical temperatures, discovered that these samples were capable of almost completely canceling the magnetic field inside the material. Moreover, unlike a perfect conductor, when these samples were first kept at temperatures above the critical point and subjected to an external magnetic field and then subsequently cooled, they were still able to expel the magnetic field from within once they cooled below their critical temperature. Consequently, superconductors are fundamentally different from perfect conductors.

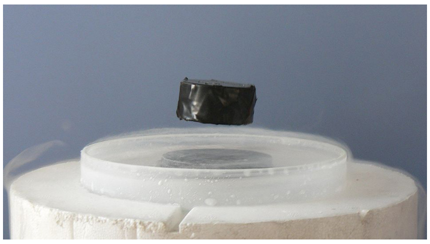

Figure 1.1: Meissner-Ochsenfeld Effect. Levitation of a magnet above a superconductor

1.2. From the first equations to the BCS theory

1.2.1. London Equations

In 1935, the London brothers developed the first equations that described the behavior of superconductors, although they did not provide a microscopic explanation of the phenomenon. By considering two populations of electrons, one consisting of superconducting electrons and the other of 'normal' electrons, and assuming the presence of a direct current, the two London equations are obtained [2]:

$$\frac{\partial}{\partial t}\left(\nabla \times \mathbf{j}_s + \frac{n_s e^2}{m}\mathbf{B}\right) = 0, \qquad \nabla \times \mathbf{j}_s + \frac{n_s e^2}{m}\mathbf{B} \;= 0 \tag{1.1}$$

With $\mathbf{j}_s$ as the current density, n_s as the density of superconducting carriers, m as the equivalent mass, e as the charge of the carriers, and $\mathbf{B}$ as the magnetic field. From these equations, I can derive the magnetic field diffusion equation and also find a new parameter that characterizes superconductors:

$$\nabla^2\mathbf{B} - \frac{\mathbf{B}}{\lambda_s} = 0 \qquad , \qquad \lambda_s \equiv \sqrt{\frac{m}{n_s e^2}} \tag{1.2}$$

$\lambda_\mathbf{s}$ is called the London peneatration depth and it gives us the degree of penetration of the magnetic field into the material. This parameter will help us later to classify the different types of superconductors.

1.2.2. Ginzburg and Landau Phase Transition

In the 1930s, Landau developed a theory of second-order phase transitions in which such transitions are characterized by an order parameter that is zero above a critical temperature and nonzero below it [3]. In 1950, Ginzburg and Landau postulated an order parameter for the superconductor transition, ψ, which, similarly to the order parameter in the superfluid helium transition, was assumed to be complex and position-dependent. [4]

$$\psi = |\psi| e^{i\phi(r)} \tag{1.3}$$

By expanding the free energy of the superconductor around that of the normal state and minimizing the free energy difference between the superconducting and normal state, we can determine the equilibrium value of ψ. At that time, the meaning of was not well understood; however, years later, Gorkov was able to derive the Ginzburg–Landau theory from the BCS theory and clarify its physical interpretation, for example, establishing that

$|\psi| = \sqrt{n_s}$, with n_s as the density of Cooper pairs(We'll explain the Cooper Pairs in the next subsection 1.2.3). Moreover, if we consider the interface between a normal metal and a superconducting metal, we can obtain a one-dimensional model and also identify a new parameter that characterizes superconductors.

$$\psi(x) = \psi_0 \cdot tanh(\frac{x}{\sqrt{2}\xi}) \quad , \quad \xi(x) \equiv \sqrt{\frac{\hbar^2}{2m^* \cdot |a(T)|}} \tag{1.4}$$

where x denotes the spatial coordinate along the x direction; $\psi(x)$ is the position-dependent order parameter; ψ_0 is the bulk value of the order parameter; T is the temperature; $\hbar$ is the reduced Planck constant; m^* is the effective mass of the superconducting carriers; and $a(T)$ is the temperature-dependent Ginzburg–Landau coefficient of the quadratic term and $\xi(T)$ is the **Ginzburg-Landau Coherence Lenght** and is a measure of the distance from the surface over which the order parameter has recovered back to nearly its bulk value.

The ratio of the London penetration depth to the Coherence length yields a temperature-independent parameter and thus describes an intrinsic property of the material: $k = \frac{\lambda(T)}{\xi(T)}$. Depending on its value, we can identify type I and type II superconductors. The former have a single critical field at which superconductivity disappears; the latter have two: a lower critical field Hc_1 and an upper critical field Hc_2. For fields below Hc_1 they behave like type I, but if we apply a field greater than Hc_1, superconductivity is not completely destroyed, unlike in type I. Instead, for fields between Hc_1 and Hc_2 the system is in the Abrikosov (mixed) regime, a transitional state before superconductivity vanishes entirely.

1.2.3. The advent of the BCS theory and the long-awaited microscopic explanation of superconductivity

In 1950, Emanuel Maxwell, at the National Bureau of Standards, used a sample of Hg^{198} that was 98% pure to conduct experiments aimed at measuring the critical temperature of this sample [5]. He discovered that compared to natural mercury (which has a higher atomic mass than the 198 isotope), there was an increase in the critical temperature. From this study, the following relationship emerged: $T_c \propto \sqrt{\frac{1}{M}}$, where M is the **Isotopic Mass**. This provided a strong indication that phonons might be involved in superconductivity, given that lattice vibrations are likewise inversely proportional to the atomic mass.

In 1957, the development of a microscopic description of superconductivity was finally completed thanks to physicists Bardeen, Cooper, and Schrieffer[6]. Cooper theoretically demonstrated that two electrons (which normally repel each other due to Coulomb forces) can bind together in a solid, regardless of whether the attractive force is weak or not. These bound electron pairs are known as Cooper pairs. In the specific case of conventional superconductors, this attractive force originates from the electron-phonon-electron interaction, in which one electron emits a phonon that is subsequently absorbed by another electron. To better visualize this interaction, we can imagine that as an electron moves through the crystal lattice, it attracts positive ions, creating a local excess of charge. If this charge accumulation occurs more slowly than the motion of the electrons, a second electron can feel an attraction toward the region where the positive charge has accumulated. In any case, the interaction potential can be approximated by the following expression:

$$V_{eff}(\omega) = |g_{eff}| \frac{1}{\omega^2 - \omega_D^2} \tag{1.5}$$

Where ω is the energy of the electrons being considered, ω_D is the Debye frequency and g_{eff} is the effective electron-phonon coupling, which is proportional to $\sqrt{\frac{m}{M}}$, where m is the effective mass of the electrons at the Fermi surface and M is the mass of the ions. In BCS theory, only electrons within an interval around the Fermi surface $\pm k_B T$ are considered. Consequently, an upper limit is imposed on the value of $|\omega|$ and, at low temperatures, the potential is always negative, which means it is attractive.

Subsequently, Bardeen hypothesized that Cooper pairs, by binding together and acting as bosons, condense into the same state, sharing the same wave function, similar to what occurs in superfluids. Using the BCS theory ones can find also the energy of the ground state of the BCS coherent state and as we can see in the plot1.2 the "addition" of an unpaired electron to the BCS ground state makes possible the occupation of one-particles states which lie at least Δ above the BCS ground state energy, so this Δ is my gap in the excitation spectrum. The energy to split a Cooper pairs is instead equal to 2Δ. From the BCS ones can know also that Δ depends on temperature and one of the most astonishing predicted results of BSC theory was:

$$\frac{\Delta_0}{k_B T} = 1.764 \tag{1.6}$$

With Δ_0 as the energy gap at $T = 0K$

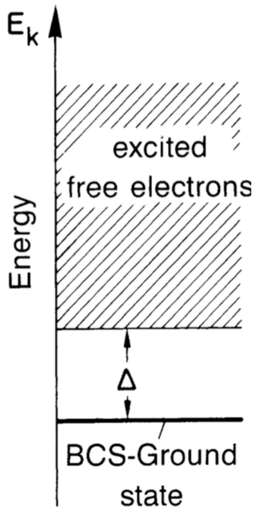

Figure 1.2: Simplified representaion of the excitation spectrum of a superconductor on the basis of one-electron energies E_k, from [7]

In 1968, McMillan [8], using the BCS theory, found that the maximum critical temperature for an electron-phonon superconductor was $T_c = 28\ K$. This result clearly set a technological limit on the widespread use of superconductors. Although it seemed that everything about superconductors had already been discovered, in the end, as in the best films, a plot twist completely overturned the situation.

1.3. The First High-Temperature Superconductor

In 1986, Bednorz and Müller discovered that $LaBaCuO_4$ was a superconducting material [9], which was surprising for two reasons: Because prior to this discovery oxides had not been considered as candidates for being superconductors and because the critical temperature presented was higher than that theorized to be the highest temperature of superconductors based on the electron-phonon interaction, that is, $T_c = 35\ K$. The main characteristic that separates cuprates from conventional superconductors was the fact that according to the BCS theory, when you are just above the critical temperature, the material must be a metal [6]; instead, Cuprates are not only not metals, but they have very strange behavior, as we will see later. Later, other superconductors with critical temperatures higher than the boiling point of nitrogen $T = 77\ K$ were introduced, making them easier to use than conventional superconductors that needed helium, which is more expensive. A material of this kind was discovered in 1987 by researchers Wu, Ashburn et al [10], it had a different stoichiometry and was the $YBa_2Cu_3O_{6+x}$, also called YBCO, a cuprate was obtained which has a critical temperature of $T_c = 92\ K$. The latter compound will be the subject of our study.

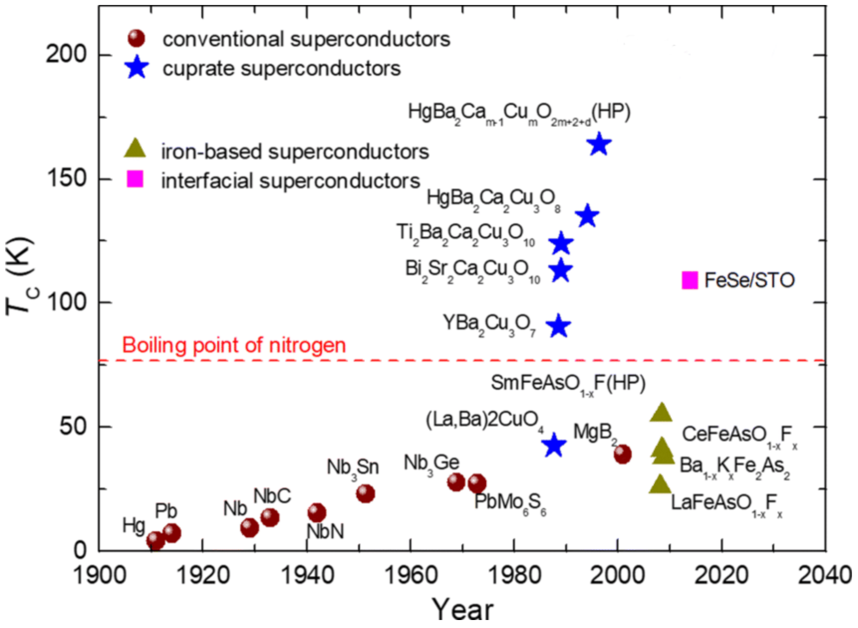

Figure 1.3: Critical temperature as a function of the discovery time of several superconductors, from [11]

1.4. YBCO

As mentioned before, YBCO exhibits a superconductivity that is not explained by BCS theory; this is due to the complex structure it presents, and one will see that the superconductivity depends on the quantity of oxygen that is present per Unit Cell. The oxygen added is a hole doping as will be explained in the next subsection.

1.4.1. Unit Cell

The $YBa_2Cu_3O_6$, the so called parent compound of YBCO (here in $YBa_2Cu_3O_{6+x}$ with $x = 0$), has a tetragonal unit cell which is composed by three perovskite units (ABX_3) stacked one a top another, where A and B are metallic cations in the center and the corners of the cube respectively.

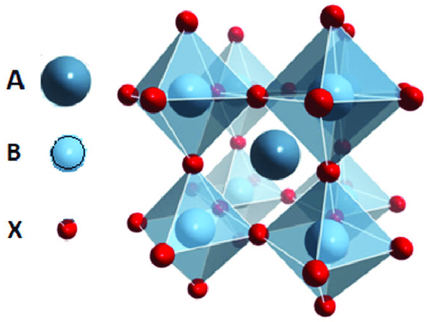

Figure 1.4: Perovskite Unit ABX_3. In this case yttrium and barium correspond to the A sites, copper to the B sites and oxygen to the X sites. Taken from [12]

The upper and lower perovskite units contain Barium atoms in the center while the central one contains a Yttrium atom; the copper atoms, on the other hand, are located at the corners of the structure, while the oxygen atoms occupy the mid-edge positions, as shown in figure 1.5.

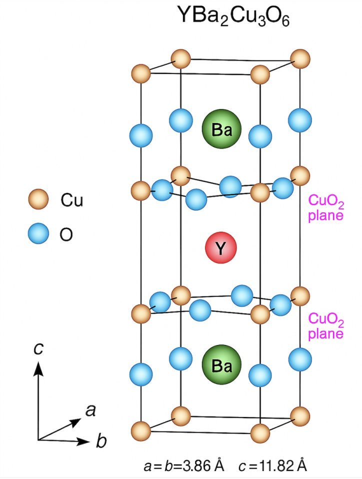

Figure 1.5: $YBa_2Cu_3O_6$ Unit Cell; in this case the a and b (the lattice axis) are equal.

The perovskite unit in the middle—namely the one containing the yttrium ion—has CuO_2 planes above and below it as shown in figure 1.5. The CuO_2 planes form a two-dimensional copper oxide layer structures which are separated by an ionic, electronically inner buffer layer as shown in figure 1.6. In the stoichiometric parent compound, each CuO_2 unit cell hosts an odd number of electrons. The states of the CuO_2 unit cells are sufficiently well localized—behaving like isolated atoms—to require a very large energy to move an electron to another site, thereby creating an "electron traffic jam." This state is also referred to as a Mott insulator. The electron spin is a dynamical degree of freedom and the virtual hopping of these electrons produces an antiferromagnetic interaction,due to the Pauli exclusion principle, which in turn generates a Nèel ordered phase [13].

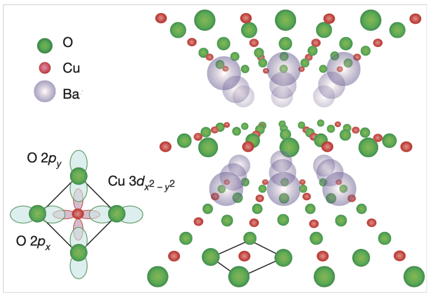

Figure 1.6: Layered copper oxides are composed of CuO_2 planes, typically separated by insulating spacer layers. Taken from [13]

If one adds more oxygen until obtaining $x = 1$ in $YBa_2Cu_3O_{6+x}$ a fully oxygenated YBCO is obtained. The $YBa_2Cu_3O_7$ has an orthorhombic unit cell; here, the added oxygen will arrange along the [010] direction and therefore the Cu and O atoms on the top and bottom of the YBCO unit cell form two parallel chains to the b axis [14]. These chains cause anisotropy in our unit cell and are known to serve as charge reservoirs. Each CuO_2 layer is connected to the adjacent layer along the CuO chain through the apical O(4) atom figure 1.7, the latter allows a charge transfer between the CuO_2 planes and CuO chains. Electrons leave the CuO_2 planes because they're attracted by the CuO chains, leaving mobile holes behind; specifically, the oxygen in the CuO chains attracts them, that's why adding Oxygen results in hole doping. This interaction is the main cause of the distortion of the tetragonal unit cell that transforms it to the orthorhombic one, in this case $a < b$, with $a = 3.82$ Å, $b = 3.89$ Å and $c = 11.68$ Å.

The CuO_2 planes are therefore metallically conducting, and the holes in the plane can condense to form Cooper pairs when T drops below T_c [14].

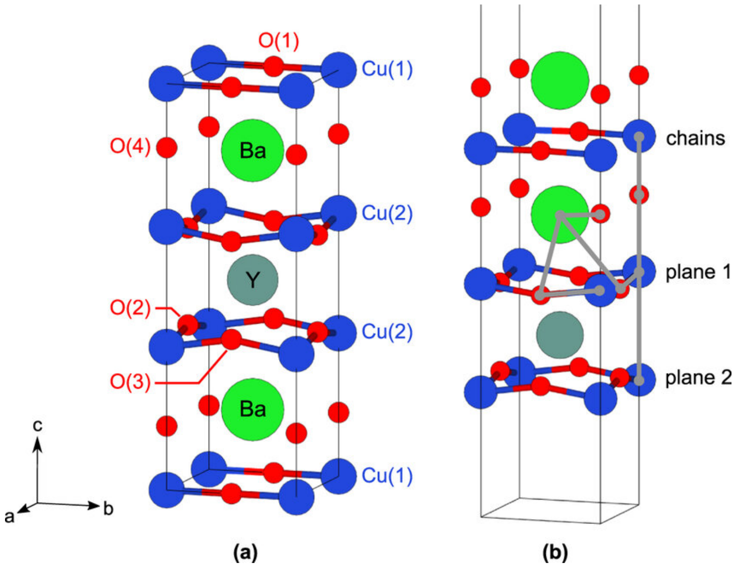

Figure 1.7: (a) YBCO unit cell. Cu(1) and O(1) copper and oxygen in the chains, Cu(2) copper in the CuO2 planes, O(2) and O(3) oxygens in the CuO2 planes in the a and b directions respectively, O(4) oxygen in the barium plane. (b) YBCO unit cell in the slab model.

1.5. Phase Diagram

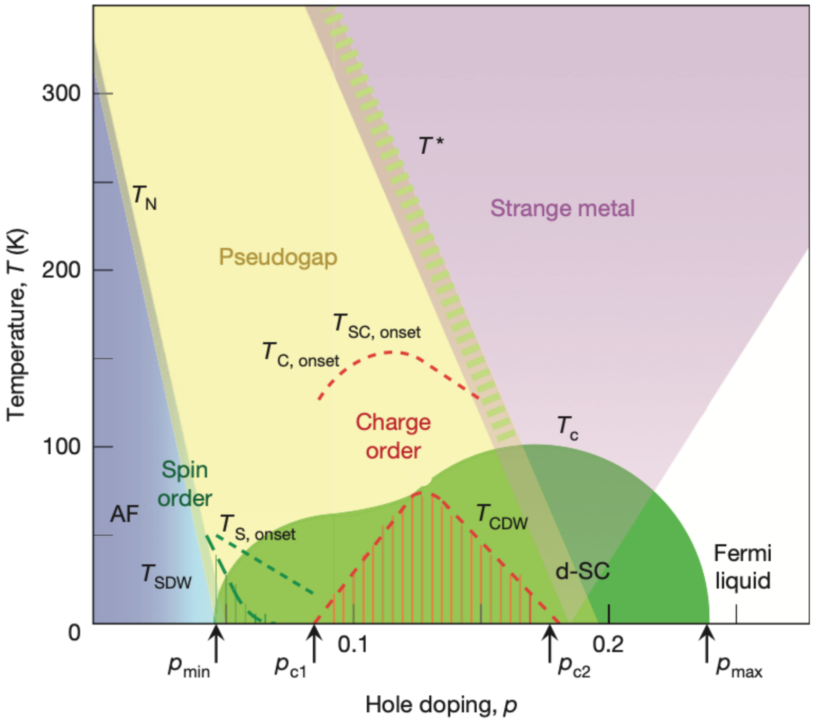

Figure 1.8: Temperature versus hole doping level for the copper oxides

The quantity of oxygen in the YBCO changes not only the structure but also its physical features; for this reason, one can use a phase diagram that depends on the temperature and the hole doping. In the phase diagram, we use p as the number of oxygen per planar copper atom. One can notice that the phase diagram is very complex and has different phases.

The **Superconductivity** zone is delimited by the critical temperature T_c and it's present in this doping range $0.05 < p < 0.27$. It seems to have a parabolic shape, but around $p \approx 0.125$ it has a deviation from this behavior; the cause could be the competition between different orders. At $p = 0.16$ we should have the maximum of the parabola; this point is known as the optimal doping, the zone after that point is defined *overdoped* zone and the zone before is called *underdoped*.

YBCO is a type II superconductor; therefore, since it has two magnetic critical fields, completely removing superconductivity requires fields over 100 T. Another difference between YBCO and conventional superconductors is that the conventional superconductors have a superconductive energy gap that is isotropic because their superconducting wavefunction has an s-wave symmetry in the momentum space, due to the fact that electrons pair in a spin-singlet configuration with $S = 0$ and $l = 0$. In the unconventional superconductors, such as YBCO, one can notice a d-wave symmetry, so the paired electrons are also in a spin-singlet state but have an antisymmetric wave function, with $S = 0$ and $l = 1$, and that means that we have an anisotropic gap. As shown in figure 1.9 one can see that the sign of the phase changes sign upon rotation by 90°. In fact, the gap has a dependence of this type:

$$\Delta(\mathbf{k}) = \Delta_0 \cos(2\theta) = \frac{\Delta_0}{2}(\cos k_x - \cos k_y) \tag{1.7}$$

Where θ is the angle in the space moment. From this relation, one can see that the gap disappears in the Nodal Points, which correspond to $k_y = k_x$ and $-k_y = k_x$, see the red points in figure 1.9. The maximum gap lie along the crystal axes in the Antinodal Points.

A first approach to study cuprates oxides used the Hubbard model and if one analyzes the approximated solution of the doped Hubbard model, one can notice that the solution points to a d-wave superconducting ground state [13].

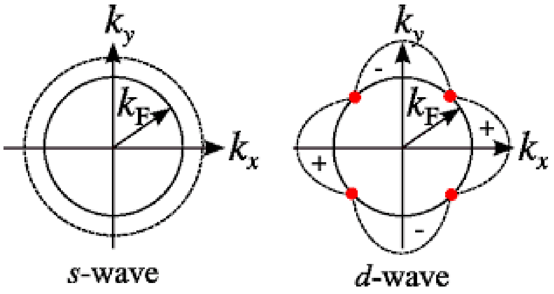

Figure 1.9: s and d symmetry in the momentum space, where k_F is the Fermi wave-vector

Before, in the subsection 1.4.1 it was explained why there is an **Antiferromagnetic** state at zero oxygen doping and, as can be seen in the phase diagram, it is present for doping levels ranging from $p = 0$ up to nearly 0.05.

Typically in the Fermi Liquid theory, which describes the normal metal state, the electron-electron interactions give rise to a T^2 dependence of the electrical resistance, and for high temperature, it saturates to a certain value when the mean free path, l, becomes of the order of the electron de Broglie wavelength λ. In the phase diagram, we can identify a small region that has this behavior and therefore it is the region where the **Fermi liquid** is present; it is localized in the overdoped zone at very low temperature (White Region in figure 1.8).

The **Strange Metal** phase is represented by the lilac region and, as shown in figure 1.8 it spans a very wide range of temperatures and hole-doping levels. In this phase, the electrical resistance has a linear T dependence from the T_c until higher temperatures, even when the mean free path l of the electron would be smaller than its De Broglie wavelength, apparently violating the Heisenberg Uncertainty Principle of the quasi-particles. It is used the word "apparently" because, in fact, in the electronic spectrum we no longer have the peaks of quasi-particles, so this is probably a strongly correlated electron system and the description of quasi-particles in the Fermi Liquid is no longer adequate. Analyzing the Strange Metal phase in the over-doped range, we can see that it extends up to the critical temperature of the superconducting state, in the range $p = 0.16 \div 0.19$, precisely where superconductivity is strongest, suggesting that these two phenomena may be connected; indeed, when large magnetic fields are applied to destroy superconductivity, the Strange Metal extends down to $T = 0\ K$. [15] A possible phenomenon that could explain the Strange Metal characteristics is the Quantum Phase Transition ruled by quantum fluctuations, which occurs at zero temperature and depends on another parameter, in our case doping. In this case, we have a point that divides the ordered and disordered phase, known as the Quantum Critical Point (QCP) [16] [17]. The QCP is characterized by a spatial-temporal invariance, so we no longer have characteristic either length or time. In this case, in the spectrum, there are power law functions and spectral functions at finite temperature that are scaling functions of $\frac{\omega}{T}$, which could be understood as a dissipative energy relaxation time: $\frac{\hbar}{K_B T}$, which is the Planckian Dissipation, the hypothetical maximum rate at which energy can be dissipated. If one analyzes the phase diagram, one could hypothesize that the strange metal is identified with the quantum critical wedge associated with a QCP under the superconducting dome near the optimal doping ($p \approx 0.19$), and its continuation outside the dome is my Strange Metal State. [13] [18] [19]

The **Pseudogap** phase is delimited by the temperature T^*, and it exists below the optimal doping (that corresponds to the maximum critical temperature, T_c) also known as the underdoped zone. Unlike a normal gap where we have a range of energy where states are not allowed, here there is not a "total gap" but only in certain directions of the Fermi surface. In the overdoped range, the Fermi surface is a hole-like cylinder centered at (π, π) in the first Brilloin zone but in the Pseudogap the Fermi surface is gapped around the corners $(0, \pm\pi)$ and $(\pm\pi, 0)$ giving rise to the Fermi arcs, see **fig.1.10**. These Fermi arcs have a similar d-wave symmetry as the superconductive gap; in fact, the pseudogap appears in the anti-nodal zones of the Brillouin zones and as said before there the superconductive gap is maximum. This could be a sign that the Cooper pairs have already formed below T^*, but since we are above T_c, these pairs do not have a coherent phase.

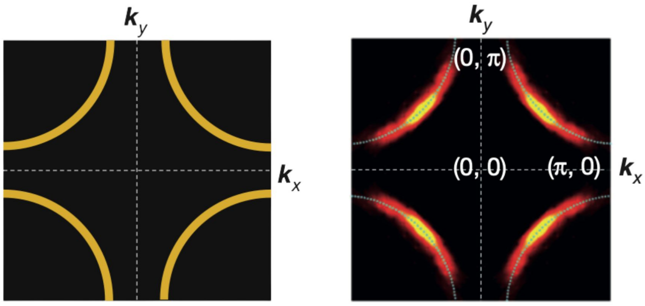

Figure 1.10: Fermi surface in the overdoped regime (on the left) and Pseudogap regime (on the right)

The resistivity of the pseudogap has a semiconductor-like temperature dependence, and this is very surprising because typically the gap increases the resistivity. Nowadays the origin of the pseudogap is unclear due to the variety of orders that are present in this regime.

Within the pseudogap region of underdoped films, a crossover from linear to purely quadratic resistive behavior can be observed. The temperature T^{**} denotes the upper bound for the quadratic dependence $R(T^2)$ and decreases linearly with increasing doping. Moreover, below $p = 0.1$, this temperature has recently been linked to the onset of electronic nematicity—an in-plane anisotropy of the transport properties that adds to the anisotropy due to the CuO chains—and whose origin remains under debate. The lower bound of the quadratic regime is set by T'. Above $p > 0.1$, T' can be associated with the temperature below which superconducting fluctuations emerge; these fluctuations affect the dc conductivity close to T_c, in agreement with microwave absorption measurements. The superconducting-fluctuation region is very narrow, though it widens at lower doping. Below $p = 0.1$, T' has been related to the metal–insulator crossover temperature [20].

1.5.1. Charge Density Wave and Charge Density Fluctuation

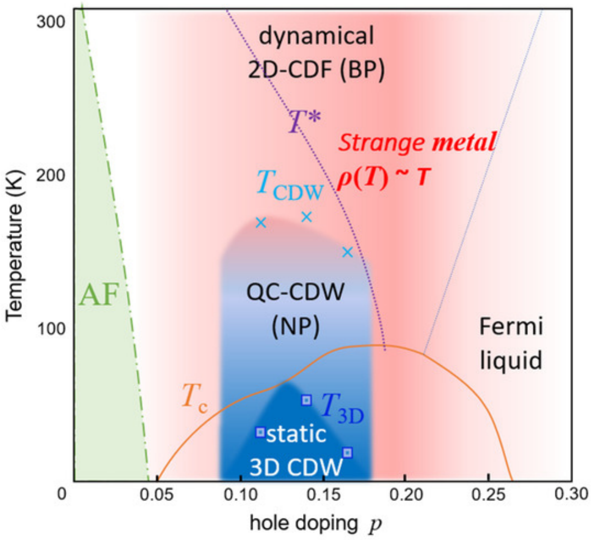

Figure 1.11: CDW in the phase diagram T vs. doping p of YBCO. The green zone is the antiferromagnetic phase. The reddish zone represents the 2D charge density dynamical fluctuations, the light blue zone is the quasi-critical CDWs and the dark blue zone is the static 3D long-range order hidden in the absence of a magnetic field by the superconductive dome. Picture took from [21] [22]

The Charge Density Wave (CDW) is a periodic modulation of charge density accompanied by a lattice distortion; this modulation could be energetically favored in a 1-D system or in layered compounds because the distortion of the lattice allows the opening of a gap that lowers the energy of electrons close to the Fermi energy. The distortion of the lattice breaks the native lattice symmetry.[23]

In the YBCO the CDWs are localized in the CuO_2 planes; they are 2-D in the a and b axes of the YBCO. The correlation length is $\xi \approx 20$ lattice constants for $p \approx 0.12$, so here there is a long-range order. In the phase diagram the CDW order is delimited by the T_{CDW} as shown in figure 1.11, so it is localized inside the Pseudogap regime. Some experiments [21] show how decreasing the temperature and entering within the Superconductive regime there is a competition between the Charge Order and Superconductive Order; this can be visualized in the plot 1.12 where there is the saturation of the narrow peak signal (blue square), which represents the CDWs, below the T_c for an underdoped sample of NBCO ($Nd_{1+x}Ba_{2-x}Cu_3O_{7-\delta}$). This competition probably causes the deformation of the $T_c(p)$ parabola; indeed, at $p \approx 0.12$ we have the peak of the CDWs and also the distortion of $T_c(p)$ parabola.

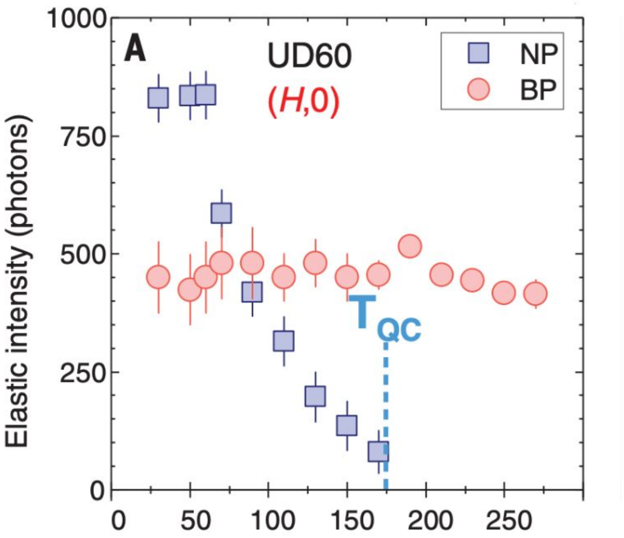

Figure 1.12: From [21]. The graph shown the temperature dependence of the parameters of the two Lorentzian profiles used to describe the quasi-elastic peaks of an underdoped sample of NBCO

The CDWs are related also to the loss of the T-linear dependence of the electrical resistivity of the Strange Metal [24]. Below the superconducting dome and under high-magnetic fields, 3D CDW's appear; in this case there is also a charge modulation along the *c*-axis; so suppressing the superconductivity there is a coupling between the CuO_2 bilayers [25] [26]. In the phase diagram they are delimited by the T_{3D} temperature as shown in fig.1.11

As shown in figure 1.11 the CDWs are limited to a small zone of the phase diagram but there is another modulation which pervades a large zone of the phase diagram and precedes the CDWs, they are the short-range dynamical Charge Density Fluctuations (CDF) [27]. In the figure 1.11 is shown how the CDF's are present in almost all the Strange Metal phase (Red Region) but also in the PseudoGap, coexisting with the CDWs, and in the Superconductive phase. CDFs compete very mildly with the Superconductive Order; one can notice that in the figure 1.12 where the Broad Peaks (red circle), which represent the CDFs, are almost constant also below the T_c [21]. They have a periodicity of ≈ 3.2 lattice units in the copper-oxide planes of cuprates, over a doping range that extends from the strongly underdoped to the overdoped regime [28]. They are characterized by an energy of a few milli-electron volts (which could produce a linear scattering rate down to 100–120 K), by a short coherence length of 1-2 wavelengths useful to scatter the low-energy electrons in a nearly isotropic way [18]. Both of these features of the

CDFs are perfect to explain the Strange metal behavior. CDW and CDF were discovered with resonant inelastic X-ray scattering (RIXS) because they produce a resonance—seen as an enhancement of the quasi-elastic spectral intensity—at a characteristic momentum transfer q given by the reciprocal of the modulation period [28]. As mentioned before, the Strange Metal can be caused by a quantum phase transition with the presence of a QCP, and in that case, the CDFs have to be maximum at the QCP and have to have a minimum characteristic energy which increases as one moves away from the QCP. In the paper [28] the characteristic energy $\Delta(T, p)$ is analyzed; this is the energy value at which the spectral density of the fluctuations related to the inelastic component observable in the RIXS assumes the maximum value for q_{CDW} and is defined as $\Delta = \frac{\omega_0(T)}{\gamma}$, where γ is the Landau Damping parameter and is proportional to the electron density of states, ω_0 is the minimum frequency of the CDFs and is correlated to their correlation length by the relation: $\omega_0 = \nu_0 \xi^{-2}$. It can be observed that Δ is minimal at $p \approx 0.19$, corresponding to the putative QCP. Moreover, the characteristic energy increases both with rising temperature and when the doping deviates from $p \approx 0.19$; additionally, the intensity of the CDFs is maximal when measured near $p \approx 0.19$; so there could be a critical wedge in the phase diagram demonstrating the presence of a QCP. In that case, however, one would expect the correlation length to diverge at the putative QCP when approaching the zero temperature, but this does not occur. Probably the superconductive order influences the behavior of the CDFs below the T_c, but also in the case that the correlation length really diverges so for $\omega_0 \to 0$, that's in contradiction with the observation of linear resistivity extension down to low temperatures in the absence of superconductivity. The reason why it would be a contradiction is that the linearity of the resistivity needs a quasi-isotropic scattering of the carriers but in this case the CDFs correlation lengths diverges. To solve this problem Δ have to remain finite for $T \to 0$ and in that case either $\Delta \to 0$ with the divergence of γ (this fact would mean that there is a QCP, and in this case, the CDFs can explain the T-linearity of the Strange Metal), or Δ doesn't tend to zero so there is a frustrated criticality.

To find out which of these cases is true, however, we need to study the CDFs below T_c without the superconducting order, but this is really difficult because to suppress the superconductivity we need to apply a magnetic field of approximately 100 T, and no RIXS facility is equipped with such a high magnetic field. An alternative solution is needed.

1.6. Zn-doping of YBCO

Typically, the YBCO is robust against increasing temperature, external magnetic fields, and disorder out of CuO_2 planes, but by contrast, Zn substituted for plane-Cu sites quite effectively kills the high-temperature superconductivity [29], and leads to a change in oxygen stoichiometry and to a local lattice distortion with the Zn cation acting as a strong scattering centre and inducing a local magnetic moment that increases with Zn concentration. It is the magnetic pair breaking that plays a main role in the suppression of superconductivity, as per the Abrikosov–Gor'kov (A–G) pair breaking theory [30].

The study and characterization of Zn-doped YBCO began in 1988; the first Zn-doped samples were fabricated using the solid state reaction where the precursors (Y_2O_3, $BaCO_3$, CuO and ZnO) powder are mixed in stoichiometric proportions and then calcined at 900°-960°[31]. With this method, ceramic samples are obtained and therefore the greatest part of the firt studies of the Zn-doped YBCO were made for this kind of samples. Different studies showed how increasing the Zinc doping an almost linear decrease of the T_c is obtained, until the complete destruction of superconductivity [32], as shown in table 1.1. The variation of the lattice parameters is almost negligible for low Zinc doping.

x (%)	a (Å)	b (Å)	c (Å)	T_c (K)
0.0	3.81	3.88	11.65	86.0
2.0	3.81	3.88	11.64	64.9
3.0	3.82	3.88	11.65	56.9
5.0	3.81	3.88	11.64	43.2
8.0	3.81	3.88	11.64	13.0
10.0	3.82	3.89	11.66	< 1.7

Table 1.1: Structural parameters and Critical Temperature of $YBa_2(Cu_{1-x}Zn_x)_3O_7$, from [32]

The Electronic Raman Scattering analysis of the 2% Zn-doped samples [33], shows how in spite of the decrease of the T_c, in the antinodal region the superconductive gap remains energetically constant; this fact is completely unexpected in a conventional superconductor.

Studies by Henri Alloul et al. [34] show that increasing disorder through the introduction of impurities such as Zinc leaves the pseudogap temperature T^* almost completely unchanged. Hence, the pseudogap regime is a phenomenon that is robust against impurity introduction, and this is evidence that the pseudogap is not a precursor to superconductivity but rather a “competitor” to it.

Another method for the production of the Zn-doped YBCO samples is the Pulsed Laser Deposition (this will be examined in depth in the next Chapter 2.1), with this, it is possible to obtain samples in the form of high-quality thin films. For this reason, we used this method for the production of our samples. However, the literature still lacks a systematic study in which zinc and oxygen doping are varied in a controlled manner.

We aim to study CDF—which peak at p=0.19, where Tc is also maximal—over a wider temperature range, avoiding competition/intertwining with the superconducting state. This can be achieved with Zn: substituting a small fraction of atoms strongly suppresses Tc. However, we must ensure high-quality films so that the observed properties are intrinsic to the Cu→Zn substitution rather than due to extrinsic sample defects. Our goal is to construct the phase diagram of these samples to track how the various regions in the superconducting and normal states evolve. Since orders such as CDW/CDF affect the phase diagram, any changes can already indicate how CDW/CDF are modified in Zn-doped samples.

In the Walker et al. paper [35] , the samples were produced in very similar conditions with respect to ours. This study shows that residual resistivity increases with increasing Zinc content in the sample. This data will be used to better understand our results since our samples are also thin films.

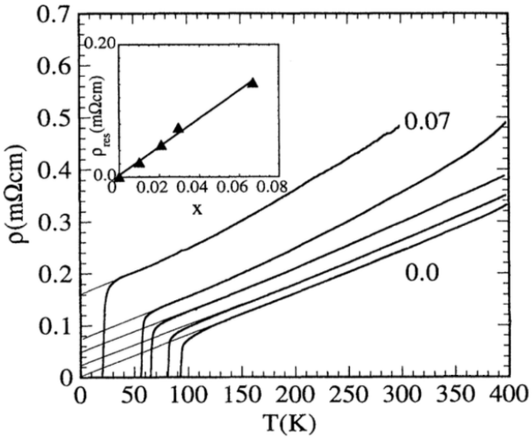

Figure 1.13: The resistivity of a series of $YBa_2(Cu_{1-x}Zn_x)_3O_{6.95}$ with x=0.0, 0.01, 0.02, 0.03, and 0.07. Taken from [35]

ARPES, STM, and RIXS analysis of Zn-doped samples are not yet available. For this reason, the purpose of this thesis is important.

2 | Methods and Instruments for Growth and Characterization

2.1. Pulsed Laser Deposition

For the groth of Zn-doped YBCO thin films, Pulsed Laser Deposition **(PLD)** was adopted because it is one of the most effective methods for growing high-quality oxide thin films, including high-T_c superconductors. A key advantage of this method is its flexibility: many growth parameters can be tuned. It is therefore preferable for our goal of spanning the entire phase diagram, particularly by varying the oxygen content. The PLD is a physical vapor deposition process carried out in a vacuum chamber (it will not necessarily be empty; sometimes there is a filled gas, in our case it is oxygen). This technique uses a high-intensity laser to produce a short pulse which is absorbed by a few atoms layer of the target, and in this way, it vaporizes or ablates a small quantity of the target, creating a plasma plume because in the skin region of the target there is the forced material ejection which, for very low pressure, will be perpendicular. At this point, we have the material flux from the target toward the substrate, which is located at a specific distance from the target to obtain a good deposition generated by the plasma plume impinging on the substrate. This process depends on multiple variables which could influence the dynamics of the plasma plume and the deposition on the substrate; for this reason, in the next subsection, it will be explained the mechanisms which govern the PLD.

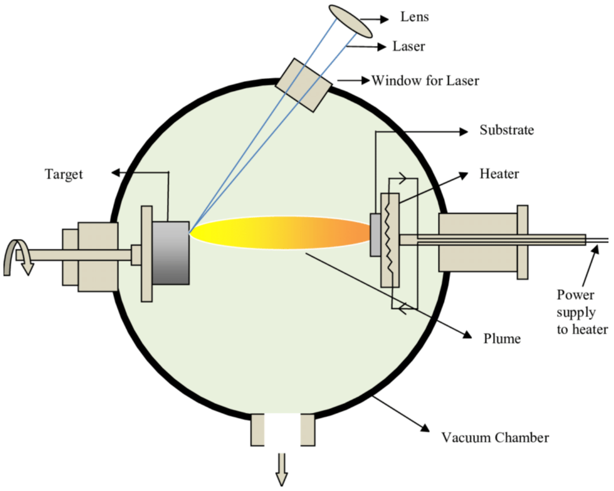

Figure 2.1: General schematic of a PLD system: as you can see, the geometric configuration is arranged so that the angle between the laser beam and the target is 45°, and the plume is perpendicular to the target and parallel to the substrate. Image taken from [36]

2.1.1. Laser-Produced Plasmas and Deposition

The performance of the High Temperature Superconductors **(HTS)** thin films depends on the surface morphology, composition, and crystallinity, which are governed by various interactions of the plasma with the background gas, the temperature, the plume geometry, and the substrate-target distance. In fact, these parameters control the dynamics of the plasma expansion and, consequently, the ejection of target material, the expansion toward the substrate, and the growth of the film, and that's why a detailed understanding of the plume dynamics is required to achieve enhanced control of the growth of complex oxide thin films.

As mentioned in the beginning of the chapter, the first step is given by the laser pulse. The main parameters of the laser which influence the plasma dynamics are the wavelength of the laser pulse, the Laser Spot Size and the Fluence of the Laser. The first parameter is important because to ignite the ablation, high energy photons are required and therefore they need a short wavelength, being inversely proportional to the energy. Furthermore, the wavelength also influences the penetration of the pulse on the surface. In this step, only a few atom layers close to the surface will absorb the momentum of the photons and because of the extremely high energy density and short duration time of a single laser pulse, the bulk material will not be able to distribute the absorbed momentum on the surface to the interior of itself, and the reaction will instead be that the material in the skin region will be thrown out into the surroundings. In a YBCO target [37], $\approx 20\ ns$ after the pulse was absorbed, the electron density near the target surface is extremely high and thus the plasma is highly collisional. At this time the expansion is higher in the longitudinal direction than the lateral direction relative to the substrate; here one notices the importance of the laser Spot Size because the smaller it is, the higher the expansion velocity and the higher the peak temperature intensity.

After $\approx$60 ns the maximum temperature is reached, but in the period between 60-200 ns and for small spot sizes, the collisions between the plasma particles and the background gas reduce the plume's temperature. Since the internal plasma pressure exceeds the chamber pressure, plume expansion continues until equilibrium is reached. For a time > 100 ns, the peak radiant intensity, which is proportional to the temperature, slightly increases with time, evidencing that the plasma-background gas interface is shifting away from the target surface. In the time range of $400 < t < 1000$ ns, the dominating interactions between the plume and the background gas cause the formation of a strong shockwave, reflection and scattering of the species formed inside the plume, the ionization of background gas atoms/molecules, and the sharpening and splitting of the plasma plume. In this time period one can notice that for small spot size the plume is more spherical, exhibits faster and stronger shock front formation, but for large spot size the shock front intensity and its lateral expansion decrease and the plume is more cylindrical; this is convenient for the Pulse Laser Deposition.

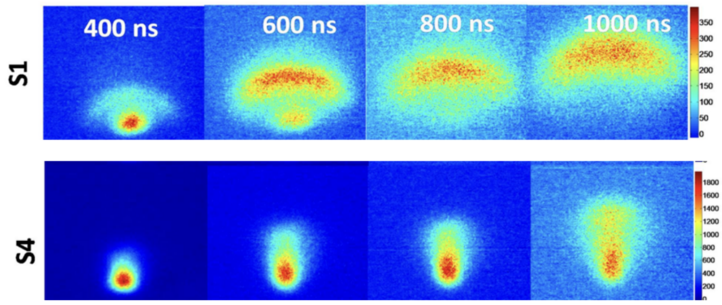

Figure 2.2: Optical images of plasma plumes, where S1 and S4 correspond to a spot size area of 0.21×10^{-4} cm^2 and 16×10^{-4} cm^2 respectively.From [37]

For a time $t > 1000$ ns the internal pressure gradient within the plume drives the expansion and the radiant emission from the plume decreases rapidly due to collisions with background gas molecules at the plume boundary and radiative cooling via recombination processes; for this reason, the plume expansion rate decreases.

At this point, the energy of the plasma plume species must be kept low using the background gas pressure, because when the high-energy species bombard the substrate surface, it could be damaged, giving rise to interstitial defects, which in turn can generate stresses in the films on the order of gigapascals (GPa).

Once the plume is fully developed and impinges on the substrate, the ablated material cloud will condense on the substrate and will form a film. If a good crystalline film is required, we need a substrate whose lattice matches the film's lattice so the film can grow epitaxially with minimal defects and it's important also to choose the right temperature at which the substrate must be heated. The substrate's choice is important because it works as a crystalline template for the growing film. The temperature is an important parameter because the condensing species will use the surface energy of the substrate to move around and find their most favorable lattice sites and because the oxygen stoichiometry has a temperature dependence, and as it was mentioned in the first chapter, the oxygen quantity within the unit cell is important for the superconductivity properties of the YBCO. The last sentence can be explained by analyzing the free enthalpy of the system **G**:

$$G = G_{perfect} + N_d(\Delta_d g + k_B T ln \frac{N_d}{N}) \tag{2.1}$$

Where $G_{perfect}$ represents the static bonding and vibrational enthalpy of the perfect crystal, N_d is the number of defects (as vacancies or interstitial Oxygen), N is the total number of crystal sites, $\Delta_d g$ accounts for the changes of the bonding and vibrational contributions due to defects. So the equilibrium defect concentration is defined by the temperature dependent minimum of G [38].

2.1.2. Calas System and DCA Cluster

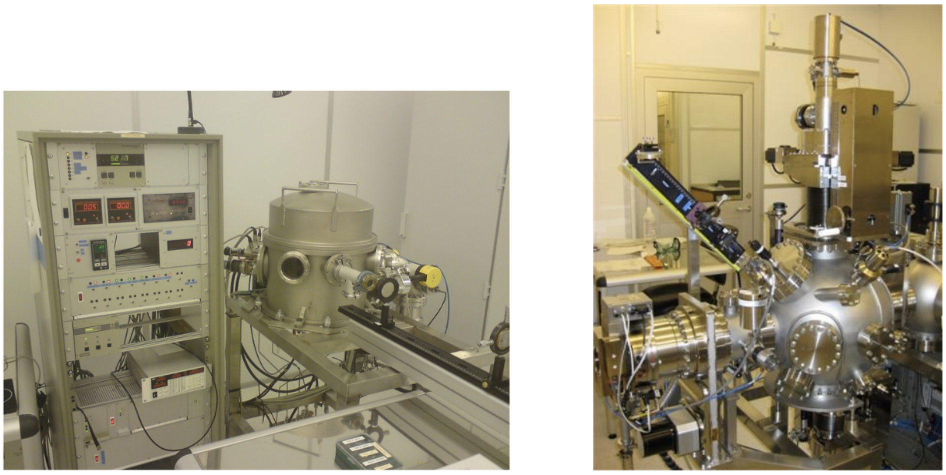

Figure 2.3: Calas System on the left and DCA Cluster on the right

For the growth of our films, we use the PLD-Calas System located in the cleanroom of the Department of Microtechnology and Nanoscience at Chalmers University of Technology. This facility—one of Europe's leading university cleanrooms—offers $1,240\ m^2$ of classified cleanroom space equipped with comprehensive processing and metrology tools, providing a broad platform for developing and testing new ideas in micro- and nanotechnology. The laboratory is also part of Myfab, the Swedish research infrastructure for micro- and nanofabrication. This system uses an excimer laser filled with Krypton and Fluorine as laser gases and neon as a buffer gas, obtaining a wavelength of $248\ nm$. The system also has a chamber where ultra-low pressures can be reached, and where different amounts of oxygen can be introduced, which is useful for deposition and post-annealing. It also includes a system for heating and cooling the sample holder. We use the Calas to obtain the slightly overdoped samples; once this type of sample has been obtained, to construct the phase diagram we need underdoped samples. Unfortunately, the range of oxygen pressure control provided by the Calas System during the annealing is not sufficient to produce these types of samples. Accordingly, we used the DCA Cluster system, which maintains highly stable oxygen partial pressures even at extremely low levels. With this setup, we can reach oxygen annealing pressures on the order of $10^{-6}\ mbar$, which will allow us to approach the antiferromagnetic samples.

2.2. X-Ray Diffraction

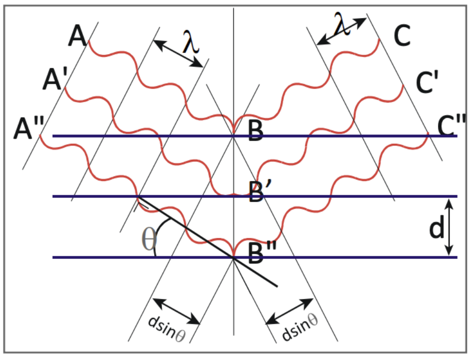

Figure 2.4: X-rays of wavelength λ impinge at angle θ on crystal planes spaced by d, illustrating the path difference $2dsin(\theta)$ and the constructive interference condition

The X-Ray Diffraction is a non-destructive method that is widely used for the characterization of thin films; it's based on the measurement of the angles and intensity of X-rays scattered off atomic layers. When the X-ray impinges on the crystal, it interacts mainly with the electrons of the atoms, generating the scattering, where the electrons re-emit the incident energy of the photons as secondary spherical waves, but since the crystal has a particular arrangement, these waves interfere with one another, producing either destructive or constructive interference. The constructive interference follows Bragg's law:

$$n\,\lambda = 2\,d_{h,k,l}\,\sin\theta \tag{2.2}$$

Where n is an integer number, λ is the wavelength of the X-Rays, $d_{h,k,l}$ is the perpendicular spacing between adjacent planes of the same family with the same Miller index (hkl), and θ is the incident angle with respect to the crystal planes.

2.2.1. Panalytical X'Pert X-Ray Diffractometer

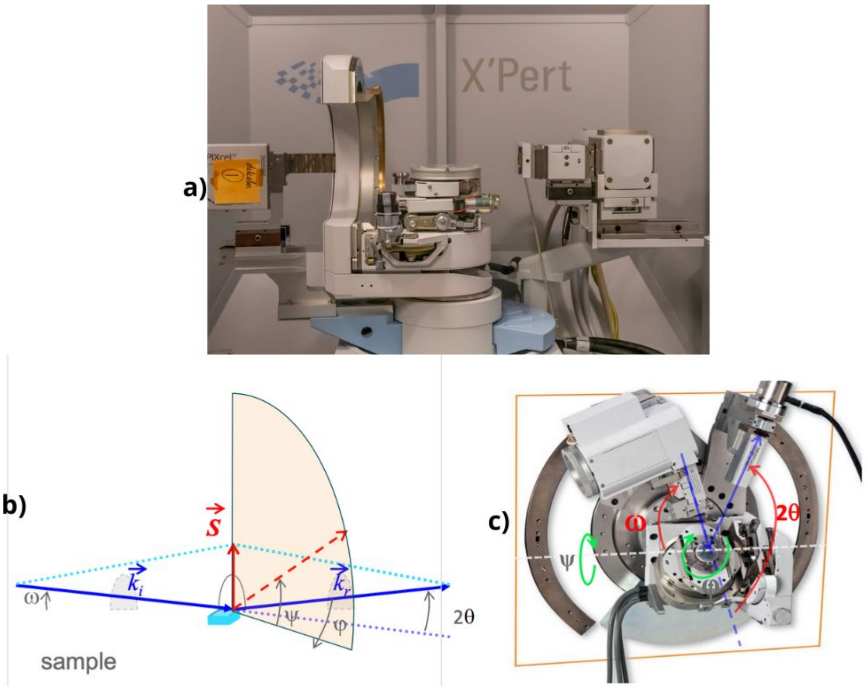

Figure 2.5: **a)**Panalytical X'Pert X-Ray Diffractometer. **b)**Schematic of the diffraction geometry used in X-ray diffraction (XRD) showing key angles: ω (angle between incident beam and sample surface), 2θ (angle between incident beam and detector), ψ (tilt angle about the axis in the diffraction plane), and ϕ (rotation about the sample normal). The incident and diffracted wave vectors, $\vec{k_i}$ and $\vec{k_r}$, and the scattering vector $\vec{s}$ are also shown. **c)**A four-circle XRD diffractometer highlighting the same rotational degrees of freedom: ω, 2θ, ψ, and ϕ, which allow detailed analysis of thin film orientation and texture.

For the XRD analysis we use the Panalytical X'Pert X-Ray Diffractometer, as shown in figure 2.5.a . It features a four-circle diffractometer equipped with various pre-aligned, fast-exchangeable X-ray optical modules. In the image, the beam from the Cu X-ray tube (CuK_α radiation) passes through a two-bounce Ge(220) monochromator that includes a mirror; the diffracted beam is then detected by a PIXcel 3D detector matrix. Among all the measurements that can be performed with the diffractometer, one of the most important is the **$2\theta/\omega$ scan**. This technique allows us to determine the crystal structure and out-of-plane orientation, allowing us to calculate the out-of-plane lattice constant and the Kiessig fringes. During this measurement, the angular setup is configured such that: $\omega = \frac{1}{2} \cdot 2\theta = \theta$, ensuring that the incidence of the X-rays on the sample always satisfies the Bragg condition.

For each peak, one can also perform a **$2\theta - \omega$ scan vs** ω, which provides information about the crystalline quality, strain, and possible defects that may be present in the film. In particular, scanning the (038) and (308) planes is essential for determining the in-plane lattice parameters "a" and "b", recalling this relationship for orthorhombic structures such as YBCO:

$$\frac{1}{d_{hkl}^2} = \frac{h^2}{a^2} + \frac{k^2}{b^2} + \frac{l^2}{c^2} \tag{2.3}$$

2.3. PPMS

Figure 2.6: Physical Property Measurement System

The Quantum Design Physical Property Measurement System (PPMS) facilitates high-precision transport measurements in both direct current (DC) and alternating current (AC) configurations. The system provides a controlled sample environment with magnetic fields ranging up to 14 T and a temperature range spanning 1.9 K to 400 K. Before measuring with the PPMS, the sample must be glued to the ETO (Electrical Transport Option) sample puck, and then the wires connecting the sample to the sample puck must be added. The electrical connections were fabricated by a wire bonding machine, which combines mechanical pressure with ultrasonic vibrations to form a solid-state joint between the wire and the pad and the thin film, obviating conventional soldering. Gold wire was used in our samples; the presence of gold pads in the thin films produced spurious reflections in the XRD patterns of certain samples and was therefore accounted for in the analysis.

3 | Growth and Characterization of Thin Films

3.1. Deposition

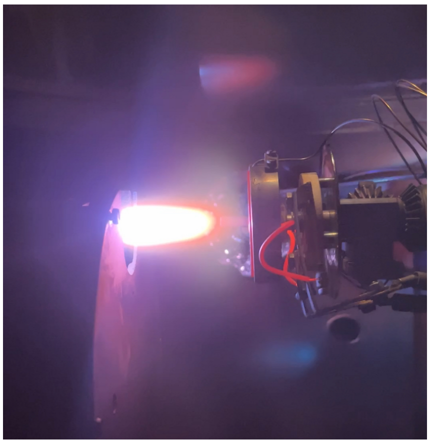

Figure 3.1: Deposition in the Calas System

The target used was the $YBa_2[Cu_{0.95}Zn_{0.05}]_3O_7$, made by SurfaceNet GmbH. It was sanded before any deposition to obtain a uniform surface where the laser pulse will impinge.

$SrTiO_3$ (001) was used as the substrate; it has a cubic structure and the lattice constant is $a = 3.905$Å, which are slightly larger than those of pure YBCO.The (001) surface is conformed by alternating layers of TiO_2 and SrO along the c-axis.

In particular, for $YBa_2Cu_3O_{(7-\delta)}$ with $\delta \approx 0$, it is possible to calculate the **Misfit**, a parameter that quantifies the difference between the in-plane lattice parameters (a, b) of the thin film and those of the substrate. In this way, the following values are obtained:

$$\begin{aligned} mismatch_a &= \frac{a_{\mathrm{STO}} - a_{\mathrm{YBCO}}}{a_{\mathrm{STO}}} = \frac{3.905 - 3.820}{3.905} \approx 2.2\% \\ mismatch_b &= \frac{b_{\mathrm{STO}} - a_{\mathrm{YBCO}}}{a_{\mathrm{STO}}} = \frac{3.905 - 3.890}{3.905} \approx 0.4\% \end{aligned} \tag{3.1}$$

As can be observed, the in-plane b-axis is practically coincident, while the in-plane a-axis also shows good agreement, In any case, both are smaller than the lattice parameters of STO (001); consequently, they are stretched and the strain is tensile. In the case of $\delta = 1$, the a and b axes are equal, leading to a misfit of $\approx 1.525\%$. This helps explain the *twinning* phenomenon: during deposition (prior to oxygen annealing), YBCO grows in the tetragonal phase, where the a and b axes are equivalent. The unit cell becomes orthorhombic once the CuO chains are formed, making the two axes (a and b) non-equivalent. If the two in-plane lattice parameters of the substrate are equal as in the case of the STO, there is no preferential direction for the CuO chains to align. Consequently, the YBCO thin film consists of crystalline grains randomly oriented along the two substrate directions, resulting in a twinned film, as shown in the paper [39].

The STO's surface matches also with the Zn-doped YBCO structure. Before the deposition, the $5mm \times 5mm$ substrate was cleaned with acetone and then with ethanol in an ultrasonic bath. Successively, the substrate was glued to the heater within the ultra-vacuum chamber, using a silver paste, checking that the distance from the target is 5 cm, since, as we have discussed, the distance from the plume is important for mass transfer. Once the chamber is sealed, the evacuation of the chamber begins; after one night we set the deposition pre-annealing parameters, these are the temperature of the substrate and the chamber pressure, the latter depending on the amount of oxygen introduced. After confirming that the laser parameters are correct, like the frequency and energy of the laser, we can begin the deposition. Once the deposition is completed, the cooling process begins at a rate of 5°C/min under the post-annealing pressure. This slow cooling promotes the full oxygenation of the chains in pure YBCO, and with the aim of obtaining slightly overdoped Zn-doped YBCO samples, it was also applied in the cases of samples 26, 27, 30, and 31.

Before selecting the reference sample for the measurements of the various parameters required for constructing the phase diagram, it was necessary to optimize the growth conditions by varying the deposition pressure and temperature. The samples presented in the table 3.1 correspond to those obtained under optimized conditions.

Sample	T_d [°C]	P_d [mbar]	E_{laser} [mJ]	f [Hz]	$P_{\text{post-ann}}$ [mbar]
R_CALAS 26	760	0.604	54.6	6	720
R_CALAS 27	760	0.602	59.9	6	700
R_CALAS 30	760	0.600	55.0	6	740
R_CALAS 31	760	0.597	55.0	6	720

Table 3.1: Parameters for the PLD. Where T_d is deposition temperature, P_d is the deposition pressure, E_{laser} is the laser energy, f is the frequency and $P_{post-ann}$ is the post-annealing pressure.

The deposition conditions used for the samples were very similar to those for pure YBCO on STO (001) and have produced good-quality films even with Zn-doped YBCO. The first sample was the R_CALAS 26, the PLD lasts 3 minutes and 20 seconds (as with all CALAS except for R_CALAS 31) and it was a good thin film; the second one was the R_CALAS 27, as shown in the table 3.1, it was deposited with a higher laser energy due to the refill of the laser gas. The R_CALAS 30 was deposited practically under the same conditions of the R_CALAS 26, it was chosen to perform the post-annealing steps and construct the phase diagram; as explained in the previous chapter 2.1.2 the deposition was carried out in the Calas system, but the post-annealing was performed ex-situ in the DCA Cluster due to the level of pressure control that can be achieved with this system. A single sample was selected to explore the phase diagram, ensuring that all observed variations can be attributed solely to changes in oxygen content rather than to spurious or extrinsic effects. The crystalline structure remains unchanged (the same sample is used), and the induced modifications are fully reversible: upon returning, after a given number of steps, to the same post-annealing pressure, the original T_c value is recovered. Furthermore, the post-annealing process in the DCA does not compromise the structural integrity of the thin film, thereby guaranteeing that changes in hole doping do not affect the reversibility of the process. It has been previously demonstrated that ex-situ annealing using the CALAS system is effective when applied to a-axis–oriented films, as reported in the referenced study [40]. In table 3.2 is shown the different annealing pressures used in the DCA Cluster, all annealing steps were carried out at 550 °C.

The CALAS_30 sample has a thickness of $\approx 60\ nm$, selected to enhance the effectiveness of the ex-situ annealing, since a very thin layer facilitates the process. The R_CALAS 31 was deposited at the same conditions of the R_CALAS 30 but the deposition time lasts 6 minutes and 40 seconds, generating a thicker film.

Annealing	$\boldsymbol{P_{\mathrm{ann}}}$ **[mbar]**
annealing 1	0.10
annealing 2	0.004
annealing 3	0.008
annealing 4	0.013
annealing 5	0.030
annealing 6	0.006
annealing 7	0.005
annealing 8	0.002
annealing 9	0.00093
annealing 10	0.00066
annealing 11	0.00040
annealing 12	0.00015
annealing 13	0.00006
annealing 14	7.90
annealing 15	75.0
annealing 16	360
annealing 17	840

Table 3.2: R_CALAS 30 at various annealing pressures

3.2. Transport Analysis

To perform transport measurements, the samples were glued to the holder and then carefully inserted into the Physical Property Measurement System (PPMS) to carry out resistance measurements as a function of temperature in a range of approximately $5 \div 300$ K. Additionally, for samples R_CALAS 27, 31, and 30, corresponding to annealings 4, 5, and 7, measurements were also performed under different magnetic fields, which allowed us to determine their critical field.

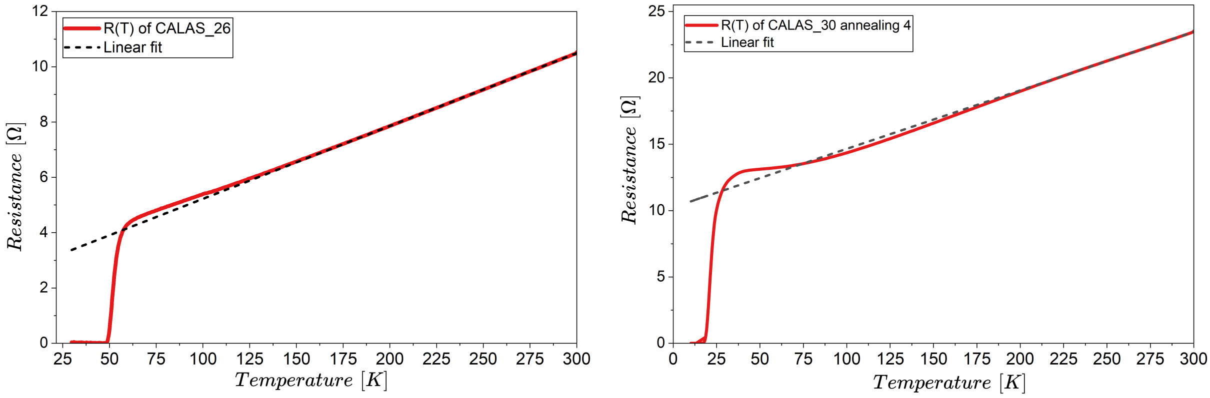

(a) R_CALAS 26, slightly overdoped (b) R_CALAS 30 annealing 4, underdoped

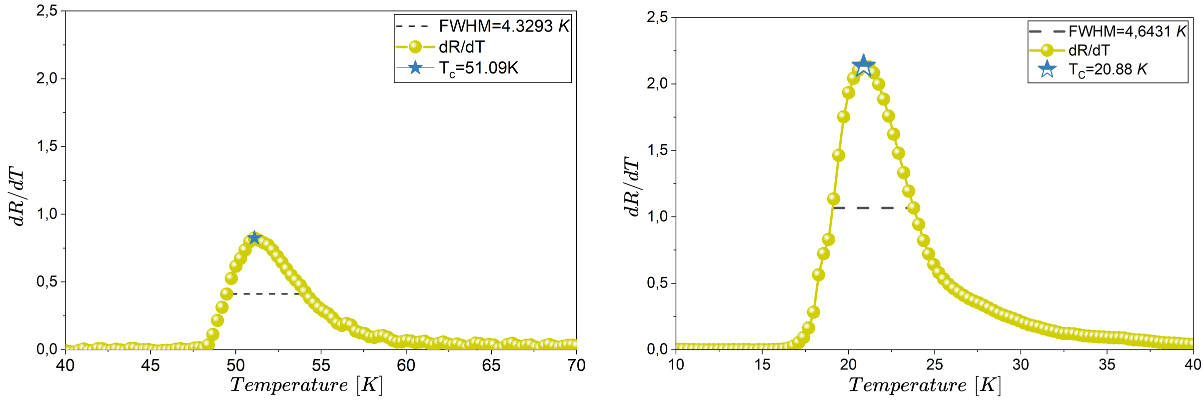

(c) R_CALAS 26, slightly overdoped (d) R_CALAS 30 annealing 4, underdoped

Figure 3.2: Measurement of the resistance of two samples with different doping levels and their respective first derivatives

From figure 3.2, it is possible to see the resistance measurement (shown in Figures 3.2a and 3.2b) of the two samples and the derivative of the resistance trend as a function of temperature (shown in Figures 3.2c and 3.2d). As shown in Figures 3.2a and 3.2b, both upturn and downturn curvatures of R(T) can be observed below the strange metal regime (linear resistance), i.e., within the pseudogap region, where a downturn curvature would be expected. This behavior originates from the parabolic (upward-curving) contribution of the CuO chains oriented along the b axis. Because our films are twinned—placing b-axis domains along both in-plane directions—the chain-induced curvature is intrinsic to our measurements and therefore unavoidable. However, this effect gradually weakens towards the under-doped regime, as the contribution of the chains becomes progressively less significant [41].

From the latter graph, it can be observed that the transition has a finite broadening, so we consider the Critical Temperature (T_c: It represents the crossover line in the $T(p)$ phase diagram below which a superconducting phase appears) as the maximum of the first derivative of the *R(T)* graph. In almost all the samples, it is possible to observe that the broadening of the superconductive transition has values around 5 K, which indicates that the films have good homogeneity. At high temperatures, as previously explained, we are in the Strange Metal regime, and consequently, the resistance exhibits a linear behavior. To determine the temperature at which this linear behavior no longer holds, a fit of the linear portion of the resistance behavior was performed, resulting in the following linear function: $R_{linear}(T) = R_0 + \gamma T$. Later we use the slope (γ) and the intercept (R_0) to plot this function $\frac{(R-R_0)}{\gamma T}$ and as shown in figure 3.3a, we can identify the temperature at which the behavior deviates from the linear trend of 1%.

Here, we must clarify the physical meaning of the temperatures marking the end of the linear regime, T_{linear}, reported in Table 3.3 . Although T_{linear} could be associated with the Pseudogap temperature (i.e., the termination of the linear resistivity), this identification is not valid in our case. As discussed above, CuO chains aligned along the b-axis introduce a parabolic contribution that obscures the true Pseudogap temperature we aim to determine. This chain-induced effect weakens as the hole-doping level decreases, making the Pseudogap signature more discernible. Consequently, in over-doped samples the temperature that marks the breakdown of the linear behavior is better identified as the Coherence Temperature, T_{coh}, a crossover temperature from a coherent to an incoherent metallic state [42]. By contrast, in under-doped samples the T_{linear} lies very close to the true Pseudogap temperature; as the hole doping is further reduced, the two become essentially indistinguishable [41].

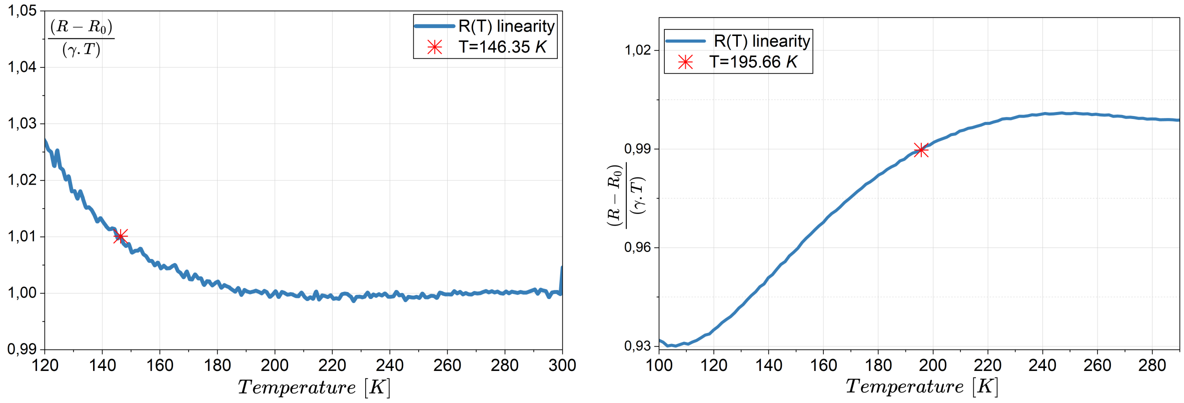

(a) R_CALAS 26, slightly overdoped

(b) R_CALAS 30 annealing 4, underdoped

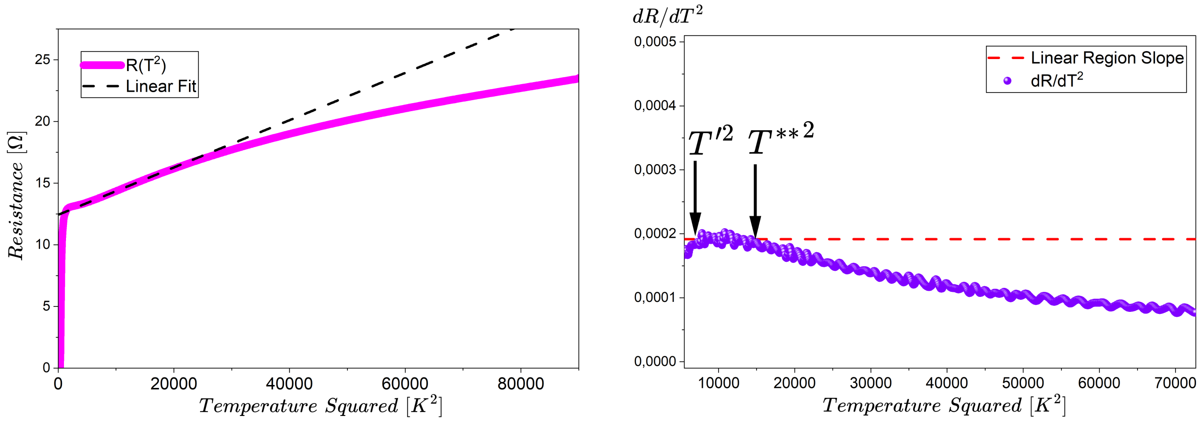

(c) R_CALAS 30 annealing 4, underdoped

(d) R_CALAS 30 annealing 4, underdoped

Figure 3.3: a), b) Deviation from linear resistance as a function of temperature. c), d) Deviation from quadratic resistance as a function of temperature squared.

For the underdoped samples, one can likewise identify a region where the resistivity shows a quadratic trend, as in Fermi liquids; this makes it possible to determine the temperature at which this behaviour starts T' and the temperature at which it ends T^{**}. To find them, the resistivity was plotted as a function of T^2, and then, using the derivative of this plot, it was checked when a linear behaviour corresponding to T' began and when it ended corresponding to T^{**}. The trend of T^{**} is very similar to that of the pseudogap temperature.

Table 3.3: Summary of the parameters. The resistivity at 100 K was calculated using this formula: $\rho_{100K} = \frac{Rt\pi}{ln(2)}$, where R is the resistance in $\mu\Omega$ and t is the thickness in cm. ΔT_c is the the broadening of the superconducting transition.

CALAS	$P\,[mbar]$	T_c $[K]$	$\Delta T_c\,[K]$	$T_{\text{linear}}\,[K]$	$T^{**}\,[K]$	$T'\,[K]$	ρ_{100K} $[\mu\Omega\,\text{cm}]$	p
30_13	0.000 06	–	–	–	–	–	17 929	0.0412
30_12	0.000 15	–	–	–	–	–	3615	0.0595
30_11	0.000 40	–	–	–	–	–	1105	0.0716
30_10	0.000 66	–	–	245.94	178.09	106.71	859	0.0770
30_9	0.000 93	–	–	245.65	166.94	112.06	780	0.0810
30_8	0.002	–	–	241.88	156.05	111.05	681	0.0825
30_2	0.004	4.61	3.1757	224.80	150.30	96.75	395	0.0815
30_7	0.005	9.75	4.1684	220.74	147.62	87.28	509	0.0880
30_6	0.006	16.25	8.7652	214.82	123.55	90.67	472	0.1025
30_3	0.008	22.26	5.3358	205.50	118.06	92.22	381	0.1158
30_4	0.013	20.88	4.6431	204.96	116.81	87.99	391	0.1140
30_5	0.03	34.40	4.7292	176.00	88.61	64.35	332	0.1330
30_1	0.1	43.45	5.2886	157.00	–	–	205	0.1430
30_14	7.9	47.75	3.1215	143.07	–	–	223	0.1575
30_15	75	48.92	2.5932	154.56	–	–	204	0.1677
30_16	360	49.20	2.0728	149.84	–	–	193	0.1728
26	720	51.09	4.3293	156.30	–	–	147	0.1900
30_17	840	49.33	5.4458	142.92	–	–	187	0.1792

Now that we have the data laid out in a table, we can compare them with those from other samples. Considering the slightly overdoped sample—which, for Zn-doped YBCO, also attains the highest critical temperature, unlike pure YBCO—and comparing it with a pure YBCO thin film deposited on STO (001) like ours [20], we observe, as expected, a decrease in the critical temperature: pure YBCO has a T_c of about 91 K, whereas our film shows a T_c of roughly 51 K. Furthermore, the pseudogap temperature of our Zn-doped sample is lower by ~ 25 K; this will be examined in greater depth in the phase-diagram section.

Paper [43] investigates a fully oxygenated polycrystalline ceramic sample with 5% Zn, matching our sample composition. That sample exhibits a $T_c = 43$ K, lower than in our fully oxygenated sample, and a narrower superconducting transition (though at 8% Zn the transition width becomes larger than in our film). The same work reports resistivity data for the fully oxygenated 5% Zn sample at various temperatures; we take the value at 100 K, which is $\rho_{100K} \approx 1463\ \mu\Omega.cm$. By comparison, our fully oxygenated film shows $\rho_{100K} = 147\ \mu\Omega.cm$, roughly one order of magnitude lower. This difference can plausibly be attributed to reduced defect incorporation and improved compositional homogeneity during growth; pulsed-laser deposition (PLD) can, in this respect, yield superior performance relative to the method used in [43].

For a more comparable case we can look at paper [35], which examined Zn-doped YBCO thin film deposited on STO at several Zn doping levels, though none exactly at 5% of Zn as in our study. To obtain a useful estimate, we took the resistance curves of fully oxygenated samples doped with 7% and 3% Zn; because the curves had the same shape, merely shifted, we extrapolated the value for a 5% Zn-doped sample. This yielded a resistivity at 100 K of 194 $\mu\Omega cm$, much closer to our sample, though still slightly higher.

By plotting the resistivity of our sample as a function of doping, as shown in figure 3.5, one notices that at high doping levels the resistivity follows a linear trend, corresponding to samples that still exhibit some superconducting phase. When the doping is reduced, the resistivity increases exponentially with doping, providing clues that we are approaching the antiferromagnetic phase. As shown in figure 3.4, plotted in logarithmic scale, two behaviors are clearly distinguishable: for $p < 0.08$ we have the exponential behavior with a higher slope and for $p > 0.08$ we have an evident lower slope.

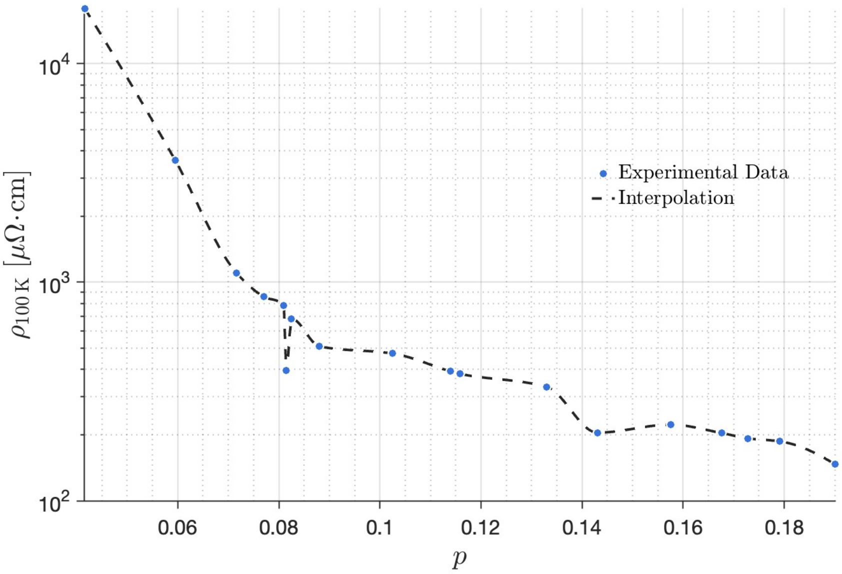

Figure 3.4: Resisitivity measured at 100K in function of the doping in logaritmic scale

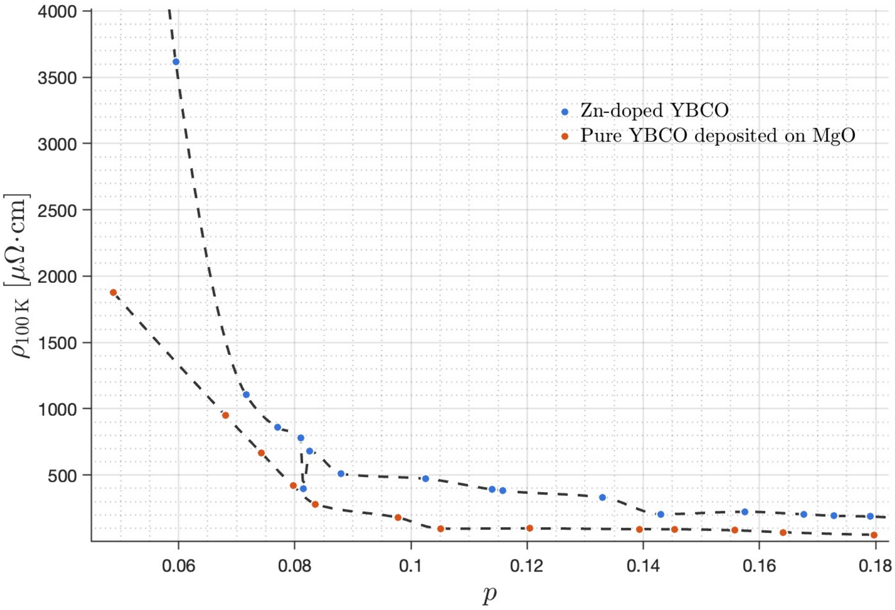

Figure 3.5: Resisitivity measured at 100 K of Zn-doped YBCO and YBCO deposited on MgO, data taken from [44]

Comparing our data with those for pure YBCO grown on MgO reported in reference [44], we observe the expected differences (Fig. 3.5). The curve for pure YBCO is slightly shifted downward; moreover, for $p < 0.08$, its slope is smaller than in our films. This behavior is consistent with Zn substitution shrinking the superconducting dome, which yields higher resistivity—at fixed hole doping and temperature—in our Zn-doped samples. For higher hole doping levels, the slope difference becomes essentially negligible.

As previously mentioned, for certain samples the resistance as a function of temperature was measured under different magnetic fields. Plotting the data, as shown in 3.6a, we can see that all the curves converge to a certain resistance value called R_N, which represents the true onset of the superconducting transition. Next, for each measurement at a different magnetic field, we looked for the temperature at which the resistance reaches a value equal to $\frac{R_N}{2}$. Subsequently, following the procedures previously adopted in refs. [45] and [46] for pure YBCO thin films, we plot these characteristic temperatures as a function of the magnetic field and as shown in 3.6b, the trend is not strictly linear, in contrast to pure YBCO. Indeed, the R^2 of the linear fit ranges from 0.910 to 0.971. This behavior appears to be attributable to Zn chemical substitution (doping). In any case, following refs. [45] and [46], we attempted to estimate the critical magnetic field—the field at which superconductivity is suppressed—by linear extrapolation.

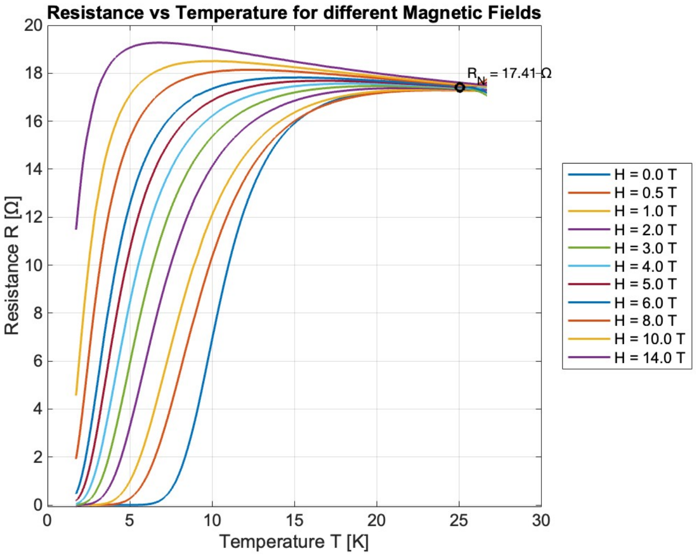

(a) Resistance as a function of temperature measured under different magnetic fields.

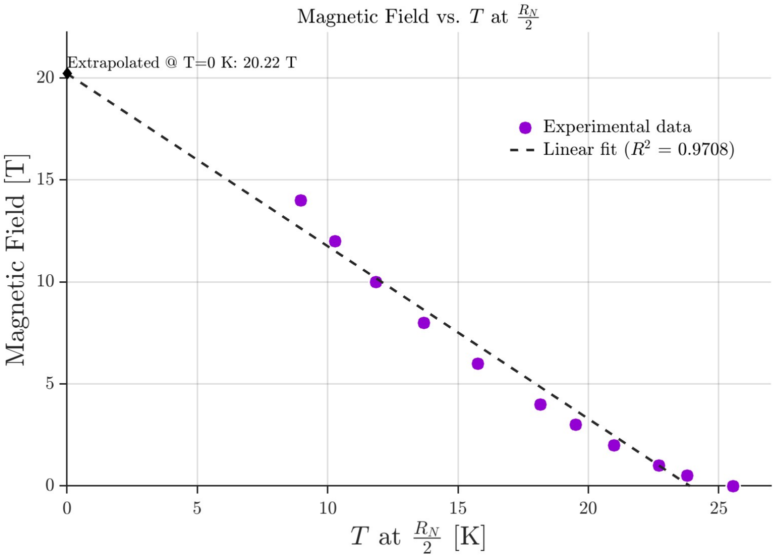

(b) Linear extrapolation used to determine the critical field.

Figure 3.6: Assesment of the critical magnetic field

Once the critical magnetic fields of the samples have been obtained, we plot them as a function of the oxygen doping (p). It can be observed that H_{c2} increases with increasing doping, with a trend that appears linear—at least within the underdoped region where our measurements are focused.”

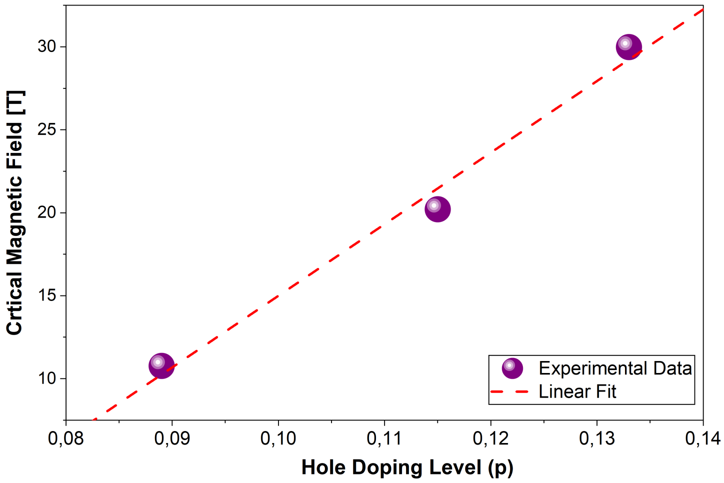

Figure 3.7: Critical Magnetic Field as a function of doping

3.3. X-Ray Diffraction Analysis

In this section, the results of the X-Ray Diffraction (XRD) analyses of the various samples, carried out using the X'Pert diffractometer presented in Section 2.2.1, will be shown. The first scan to be analyzed is the Symmetric $2\theta - \omega$ scan, which was performed over an angular range of $5° - 110°$, first in CALAS-26 and then subsequently in the following samples. As previously mentioned, the deposition was carried out under conditions similar to those used for pure YBCO on an STO (0 0 1) substrate, but it was not guaranteed that the deposition would result in a high-quality film with the desired superconducting properties. For this reason, this initial analysis was crucial for the first sample.

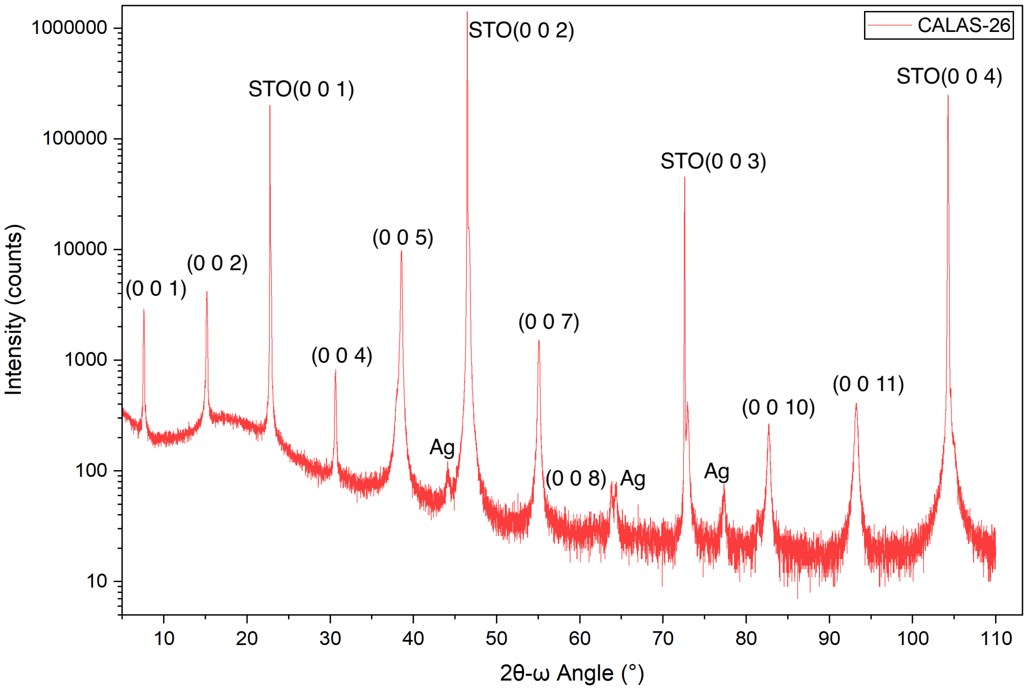

Figure 3.8: $2\theta - \omega$ Scan of the CALAS 26

In this case, the intensity has been plotted on a logarithmic scale to better visualize the peaks, while the angles are on a linear scale. In Figure 3.8, the YBCO peaks corresponding to the (0 0 l) reflections are observed, indicating a single preferred orientation with the c axis perpendicular to the substrate plane; the films are therefore c-axis oriented. In addition to the peaks corresponding to Zn-doped YBCO, we can also see the peaks corresponding to the STO, which exhibit a much higher intensity than the film and end up covering certain YBCO peaks.

As can be seen in Figure 3.8 , in addition to these peaks there are also other unusual ones. Considering that silver paint was used to attach the substrate in the Calas, the XRD pattern of silver nanoparticles was taken into account to better determine whether the peaks correspond. Our strange peaks correspond exactly to the angles 44.16°, 64.51°, 77.29° but as shown in figure 3.9 we can find similar peaks but shifted forward by approximately 2°. However, there remains a doubt in this explanation, which is the fact that the largest peak we have is at 31.87°, yet this is not present in our XRD.

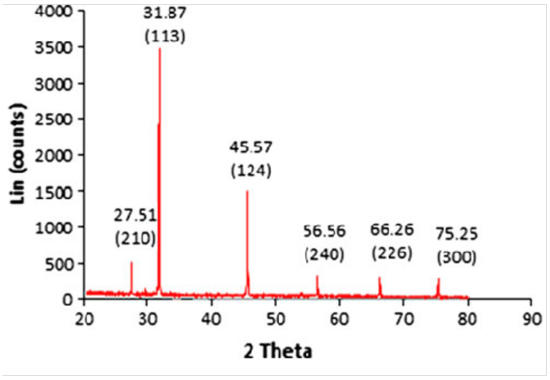

Figure 3.9: XRD pattern of silver nanoparticles. Taken from [47]

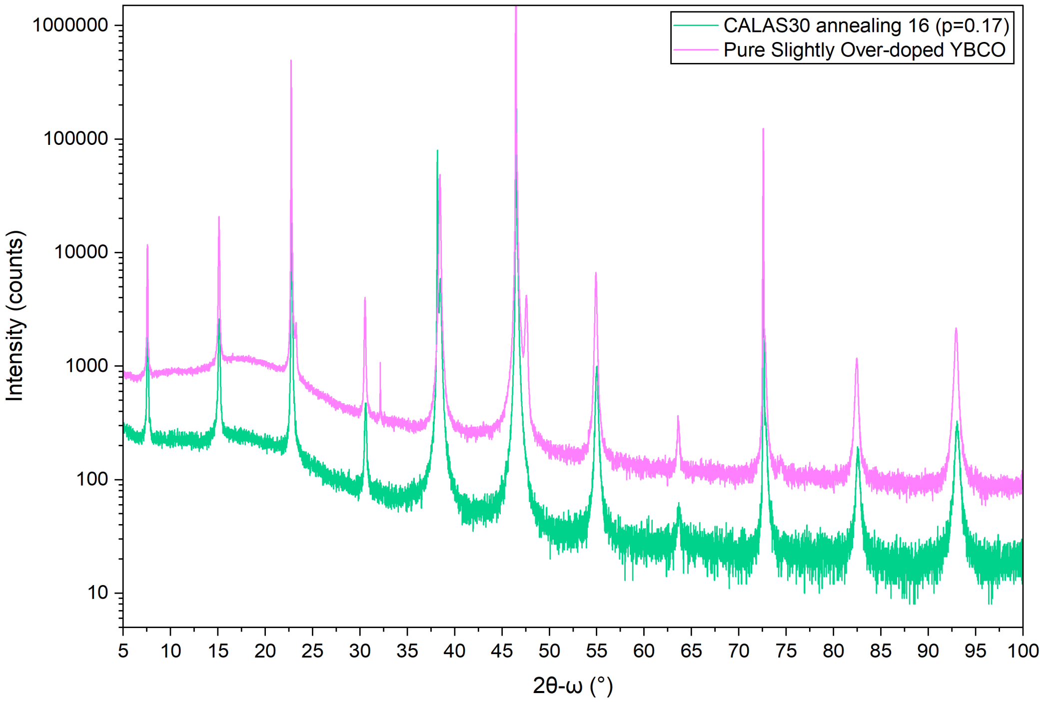

Figure 3.10: XRD pattern of Zn-doped YBCO and Pure YBCO, both deposited on STO

After confirming out-of-plane growth (c-axis orientation), we compare the XRD patterns of two samples with identical hole doping but one is a Zn-doped sample (CALAS 30 annealing 16) and the other one is made by pure YBCO, both deposited on STO (0 0 1). Figure 3.10 shows that the diffracted intensity of our CALAS 30 ann. 16 is lower and that the (0 0 l) peaks are shifted to higher 2θ. For the lowest-order YBCO peaks, the shift is approximately 0.03°, and—as also reported in Table 3.4—this offset increases progressively with the reflection order l for the greater part of the peaks. However, the fact that the diffraction-peak positions of 5% Zn-doped YBCO are nearly identical to those of pure YBCO is a strong indication that Zn substitution at this level does not significantly modify the YBCO crystal structure.

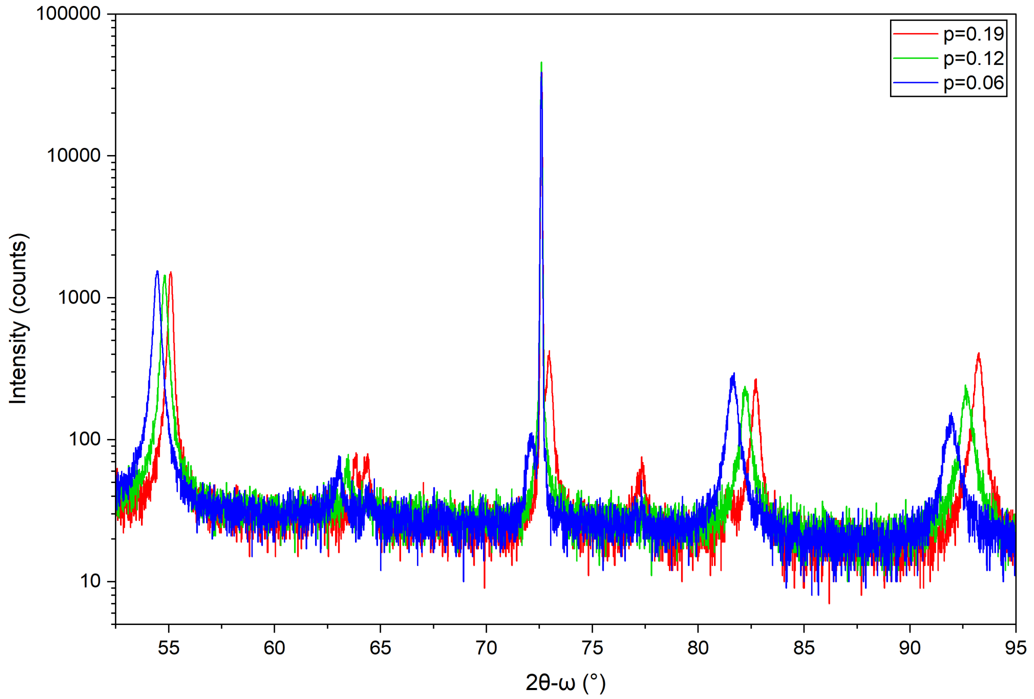

Figure 3.11: XRD pattern of several Zn-doped YBCO samples at different hole doping

In Fig. 3.11, several of our Zn-doped YBCO samples at different hole dopings are compared, where the CALAS 26 is the sample at $p = 0.19$, the CALAS 30 annealing 3 is the sample at $p = 0.12$ and the CALAS 30 annealing 12 is the sample at $p = 0.06$. As the hole doping level increases, the XRD peaks shift because the lattice parameters evolve; specifically, we observe a reduction of the out-of-plane c axis with increasing hole doping. Recall that the angles at which the (0 0 l) reflections appear are related to the out-of-plane lattice parameter c via Bragg's law as follows:

$$c = \frac{l\,\lambda_{\mathrm{Cu}\,K\alpha}}{2\,\sin\!\left(\frac{2\theta}{2}\right)} \tag{3.2}$$

The decrease in c arises from the formation and ordering of Cu–O chains along b, accompanied by the tetragonal-to-orthorhombic transition; these states are precisely those in which the contraction of c is observed [48].

Table 3.4: Comparison of peak positions of STO and Zn -doped YBCO at different hole doping levels and a Slightly Over-doped (SOD) pure YBCO sample.

Peaks	**SOD Pure YBCO**	**p = 0.173**	**p = 0.190**	**p = 0.116**	**p = 0.060**
STO (001)	22.731°	22.755°	22.764°	22.748°	22.745°
STO (002)	46.168°	46.487°	46.477°	46.474°	46.471°
STO (003)	72.579°	72.603°	72.594°	72.593°	72.592°
YBCO (001)	7.564°	7.593°	7.608°	7.572°	7.521°
YBCO (002)	15.118°	15.147°	15.176°	15.095°	15.003°
YBCO (004)	30.539°	30.611°	30.643°	30.496°	Low intensity
YBCO (007)	54.912°	55.009°	55.089°	54.800°	54.454°
YBCO (0011)	92.954°	93.038°	93.238°	92.618°	91.956°
YBCO (0013)	–	118.190°	–	117.464°	116.308°

Moreover, starting with the fifth annealing, there was contamination with gold. Since directly attaching gold wires to the sample had proven very difficult, it was decided to facilitate this attachment by sputtering gold onto the sample. However, this caused the YBCO (005) and (0010) peaks to be contaminated by those of gold, rendering them unusable for extracting the c-lattice parameter, as shown in 3.12.

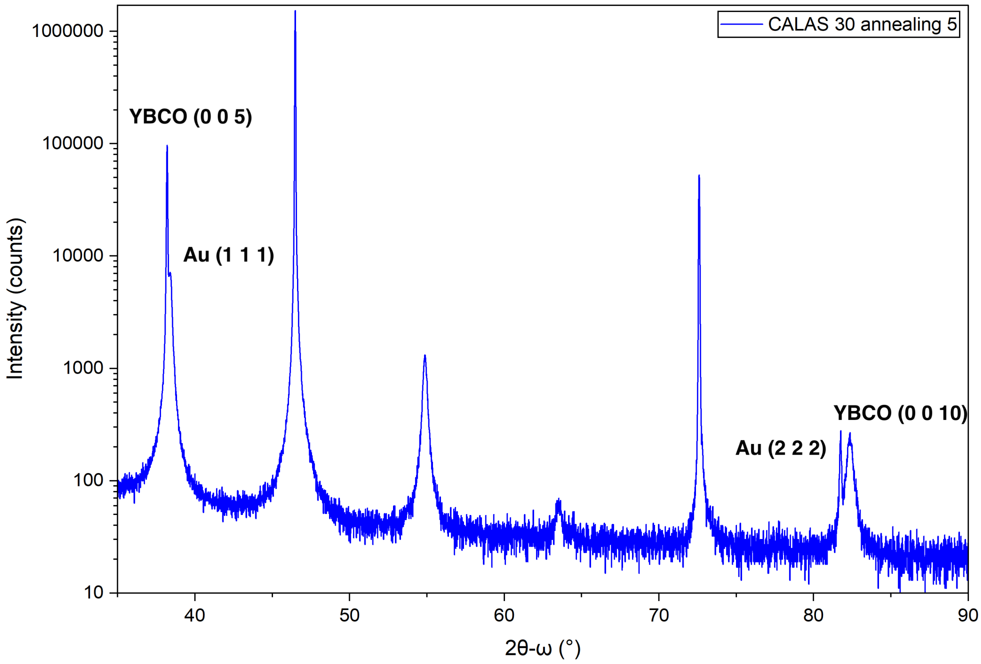

Figure 3.12: XRD pattern of CALAS 30 annealing 5

By analyzing the (001) peak of our sample, we can see interference fringes on both sides of the peak, which indicates good crystallographic quality, even though those on the left are much clearer; moreover, we can use these interference fringes to determine the thickness of our film. Once the periodic adjacent maxima around our central (001) peak have been identified, the following formula can be used to determine the thickness of our film [42]:

$$t = \frac{\lambda_{\mathrm{Cu}}}{2(\sin\omega_n - \sin\omega_{n-1})} \tag{3.3}$$

Where "t" is the thickness, "ω_n" is equal to "$\frac{2\theta_n}{2}$" which are the angles corresponding to the maxima of the interference fringes and $\lambda_{\mathrm{Cu}} = 1.540598$Å. Using this formula, a thickness of 58.2 nm was obtained, very close to the 60 nm value for the CALAS-30 annealing 16 .

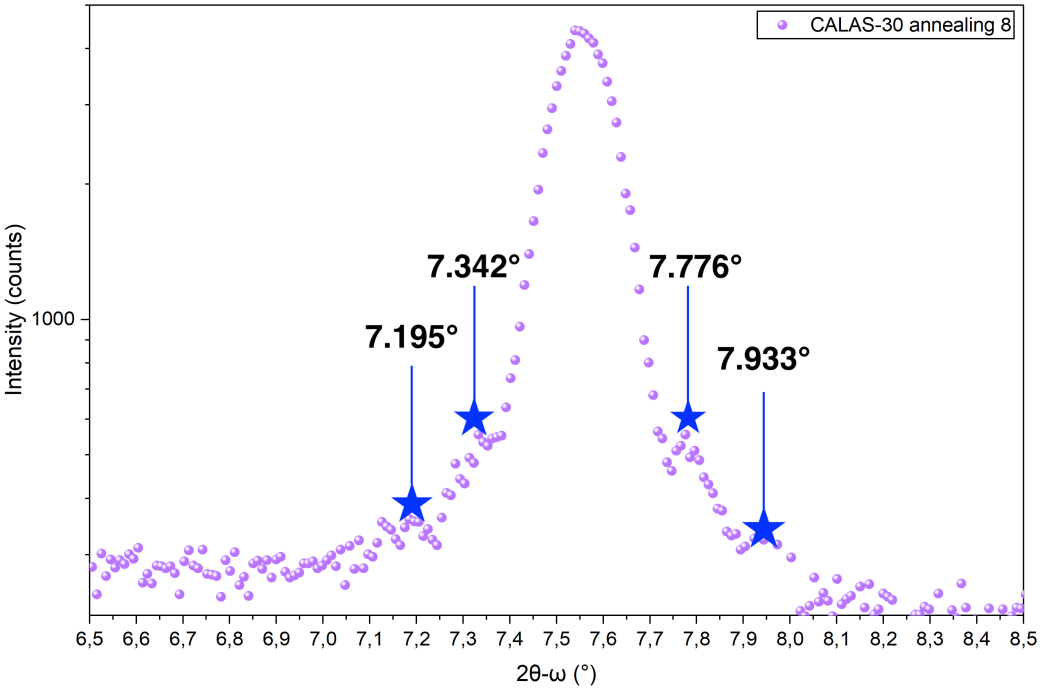

Figure 3.13: $2\vartheta - \omega$ scan of the (001) peak of the CALAS-30 annealing 8 corresponding to $p = 0.082$

Subsequently, the different peaks were normalized to the only one not obscured or overlapped by STO, silver paste, or gold—namely the (0 0 7) Bragg peak. Here in figure 3.14 you can see the different behaviors of the (0 0 l) Bragg peak intensities as a function of sample doping, which are consistent with those of pure YBCO, namely, the (0 0 l) Bragg peaks vary as a function of T_c, with distinct trends for the different diffraction orders [20].

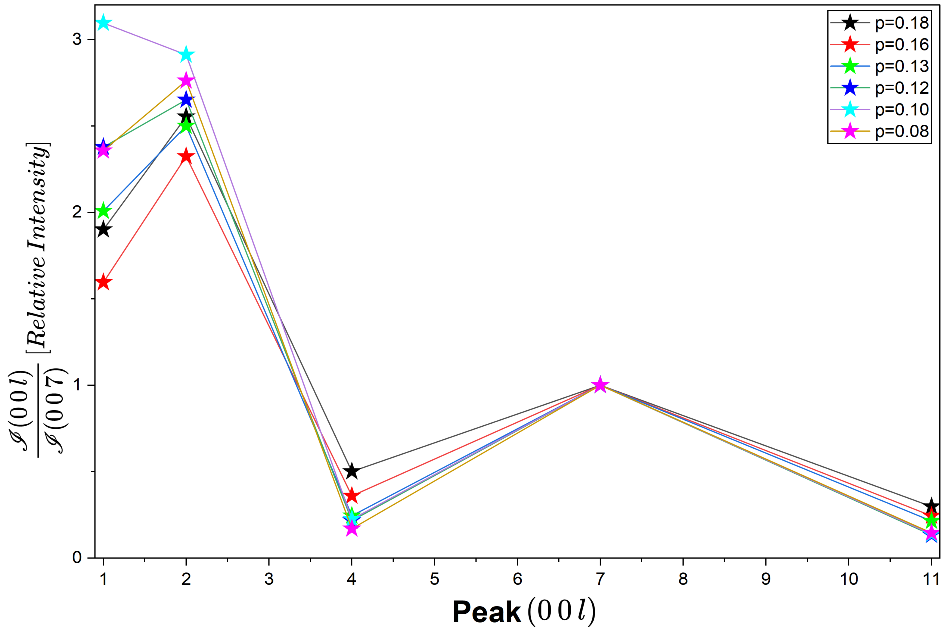

Figure 3.14: Relative change of intensity of the (00n) Bragg peak with respect to the (007) Bragg peak, in several films at different doping

Additionally, an asymmetrical $2\theta - \omega$ scan was performed, here the x-axis is 2θ, the y-axis is the variation of ω from the value $\frac{2\theta}{2}$ and the intensity is represented by the color. So for each 2θ angle we execute the scan in ω. We can use this plot to distinguish which peaks belong to the well-oriented deposited YBCO and which ones are due to silver because when the peak width in omega is limited and very narrow, it provides information about the crystalline quality and the degree of epitaxy. On the other hand, the silver particles, not being epitaxial, are very easy to identify due to their large width, as shown in the figure 3.15, where the peaks from the epitaxial crystals are narrow, while what appeared to be a peak in the symmetric $2\theta - \omega$ scan turned out to be just residual silver paint. With this initial analysis, the YBCO peaks can be identified, which will be used for the calculation of the c-axis.

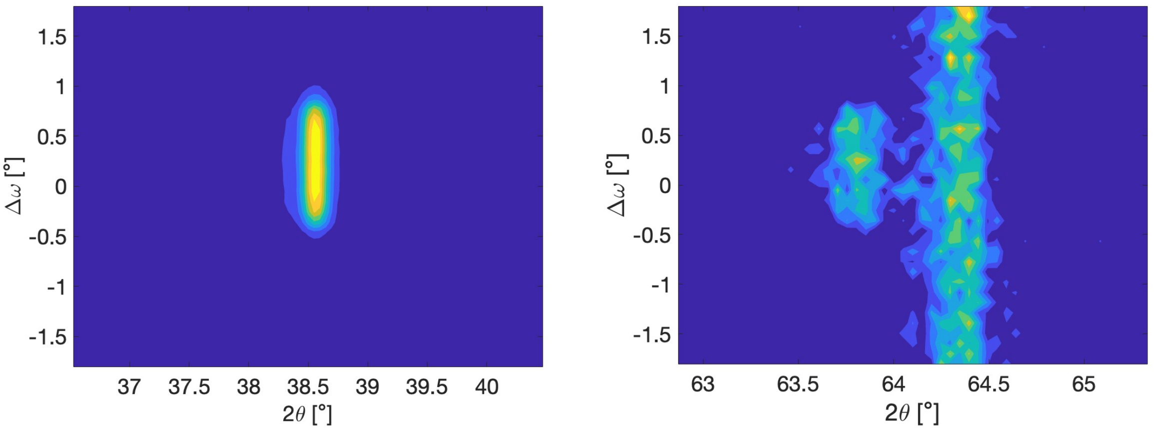

(a) Zn-doped YBCO(005) (b) Zn-doped YBCO(008) and the Silver Paint [right]

Figure 3.15: Asymmetrical $\omega - 2\theta$ scan of CALAS_26.

The asymmetrical scan can be used also to calculate the other two axes, a and b, using also in this case the Bragg's law. To find them, I need to scan the (038) and (308) planes, and then we perform a Lorentzian fit to determine the angles corresponding to the peaks of the two planes, and with that, we can use the geometric relations to find the other axis.

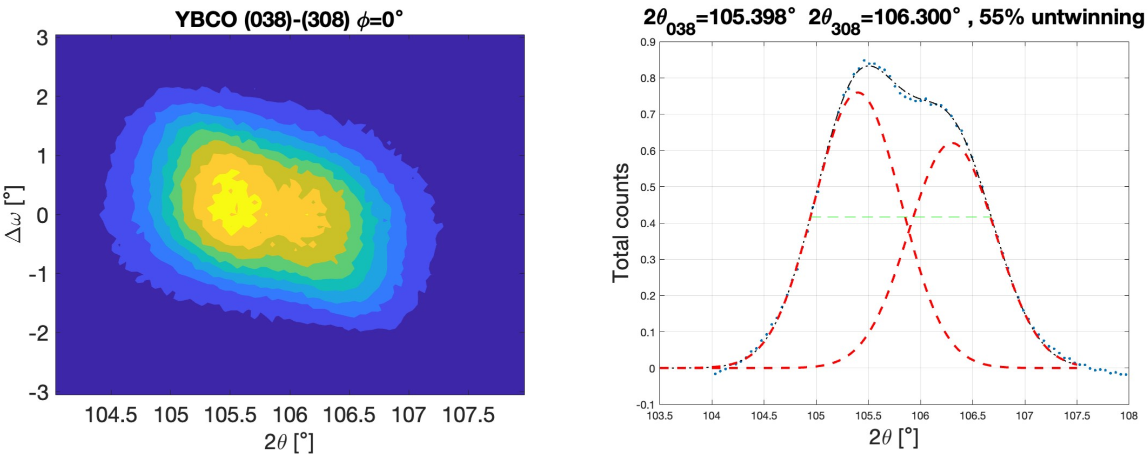

(a) Zn-doped YBCO (038) (308) (b) Lorentzian fit

Figure 3.16: Asymmetrical $\omega - 2\theta$ scan of (038) and (308) CALAS_26's peaks

In Figure 3.17 we observe that, consistent with the literature on pure YBCO, at high annealing pressure (i.e., high oxygen content) the in-plane lattice parameters a and b are markedly inequivalent due to the formation and ordering of Cu–O chains, stabilizing the orthorhombic phase. As the oxygen content decreases, the structure evolves toward the tetragonal phase, with a and b becoming nearly identical.

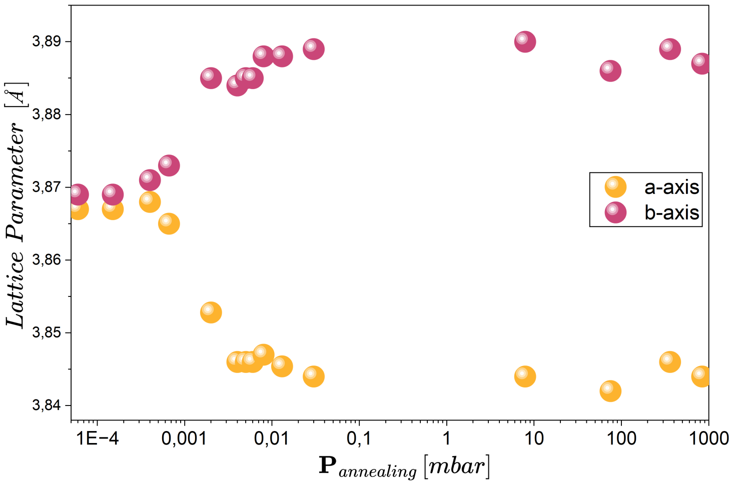

Figure 3.17: Lattice parameters a and b as a function of annealing pressure

As discussed in the beginning of the XRD analysis, as the hole doping increases, the out-of-plane lattice parameter c decreases. Accordingly, consistent with the literature, increasing the annealing pressure raises the oxygen content and thus leads to a reduction in c-axis.

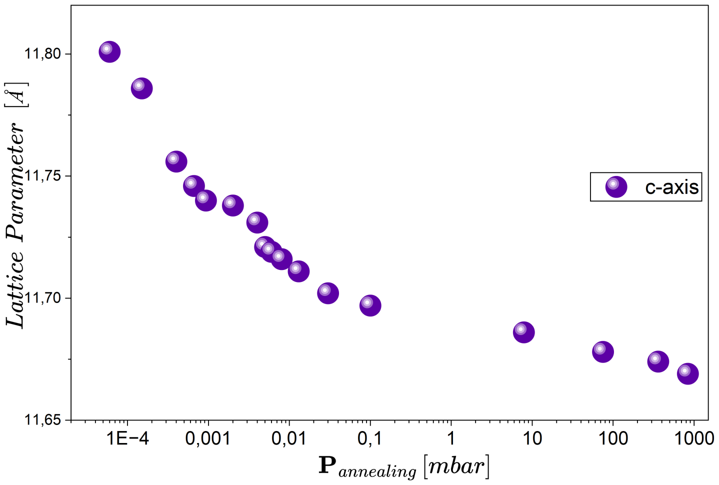

Figure 3.18: Lattice parameter c as a function of annealing pressure

In the paper [43], the sample is a fully oxygenated polycrystalline ceramic sample of Zn-doped YBCO which has $c = 11.64$ Å, $a = 3.81$ Åand $b = 3.88$ Å. It can be easily seen that both the a and c parameters are larger in our Zn-doped YBCO thin film, while the b parameter remains the same.

By contrast, the YBCO thin film deposited on STO (001) has the following lattice parameters: $c = 11.67$ Å, $a = 3.84$ Å and $b = 3.90$ Å. As can be seen, in this case the a and c parameters are practically the same as in our Zn-doped YBCO, whereas the b parameter is smaller by 0.01 Å.

Table 3.5: Summary of the Annealing Pressure, lattice parameters a, b, and c and the FWHM of the Bragg (007) peak.

CALAS	P_{ann} [mbar]	a-axis [Å]	b-axis [Å]	c-axis [Å]	$a * b$	$\Delta 2\theta$ (007)
30_13	6.00E-05	3.867	3.869	11.801	14.961	0.3125
30_12	1.50E-04	3.867	3.869	11.786	14.961	0.3184
30_11	4.00E-04	3.868	3.871	11.756	14.973	0.2964
30_10	6.60E-04	3.865	3.873	11.746	14.969	0.2978
30_9	9.30E-04	3.863	3.888	11.74	15.019	0.2820
30_8	2.00E-03	3.853	3.885	11.738	14.968	0.2988
30_2	4.00E-03	3.846	3.884	11.731	14.938	0.2781
30_7	5.00E-03	3.846	3.885	11.721	14.942	0.2811
30_6	6.00E-03	3.846	3.885	11.719	14.942	0.2827
30_3	8.00E-03	3.847	3.888	11.716	14.957	0.2734
30_4	1.30E-02	3.845	3.888	11.711	14.951	0.3048
30_5	3.00E-02	3.844	3.889	11.702	14.949	0.2901
30_1	1.00E-01	no	no	11.697	no	0.2589
30_14	7.90E+00	3.844	3.89	11.686	14.953	0.2834
30_15	7.50E+01	3.842	3.886	11.678	14.930	0.2788
30_16	3.60E+02	3.846	3.889	11.674	14.957	0.2870
26	7.20E+02	3.854	3.881	11.660	14.958	0.2456
30_17	8.40E+02	3.844	3.887	11.669	14.942	0.2662

3.4. Determination of the oxygen doping: toward the Zn-YBCO phase diagram

One of the central aims of this thesis is to compare pure YBCO with our Zn-doped samples. Specifically, we ask whether investigating charge-density waves (CDWs) in Zn-doped YBCO—within the region of the phase diagram that hosts the superconducting dome in pure YBCO—yields results that faithfully capture the underlying physics of that regime once superconductivity is suppressed. Establishing an accurate phase diagram is therefore essential to this analysis.

In order to construct the phase diagram, it is essential to determine the hole doping of our samples—a task that, unfortunately, is far from straightforward in cuprate HTS materials. In bulk crystals, chemical and thermogravimetric analyses allow precise measurement of oxygen content (by tracking the mass of oxygen atoms and its variation with critical temperature), thus yielding an accurate estimate. By contrast, in thin-film YBCO not only is oxygen content harder to determine, but even if we knew it exactly, extracting the hole concentration p remains nontrivial. Because of YBCO's crystal structure, what matters is how the oxygen atoms are distributed between the CuO_2 planes and CuO chains—only their specific locations govern the hole doping and, consequently, the superconducting properties. One of the methodologies used in pure YBCO thin-film samples to determine the hole-doping level p [20] uses the c-axis lattice parameter and the critical temperature T_c. In this case p is estimated using an empirical parabolic relation—valid only within a specific hole doping range and expressed as a function of the critical temperature T_c; the formula is:

$$1 - \frac{T_c}{T_c^{max}} = 82.6 \cdot (p - 0.16)^2 \tag{3.4}$$

In this equation T_c^{max} denotes the maximum Critical Temperature. Because the relation is strictly parabolic while the superconducting dome does not exhibit such behavior across all doping levels, it follows that it is inaccurate for determining the hole doping near $p = 1/8$ and is not applicable to strongly under-doped, non-superconducting samples. Indeed, in the regimes where this relation is unreliable, corrections have been proposed [49] that complete the relation between T_c and the hole-doping level p. Given the additional correlation between the critical temperature and the c-axis, one can therefore construct a direct relation between the hole-doping level and the c-axis, $p(c)$.

At this stage, one might consider applying the same methodology to our Zn-doped YBCO thin-film samples; however, several issues arise that are absent in pure YBCO. First, the superconducting phase disappears at relatively low hole doping, leaving many samples without a measurable critical temperature T_c across a broad range of hole-doping levels p. Second, it is not a priori guaranteed that the superconducting dome attains its maximum critical temperature T_c at the same hole-doping level p.

Having extracted the critical temperatures and the lattice parameters of the Zn-doped samples—and since the c-axis depends on the oxygen content, and also the critical temperatures depend on the hole doping—we can look for data containing these parameters to help us. In the paper [20] the plots of the c-axis length as a function of T_c for pure YBCO films deposited on MgO (110) and on STO (001) can be found. In Figure 3.19a these graphs are plotted and it shows that the two graphs have essentially the same shape. For STO (001), the curve is shifted downward—with an almost negligible leftward offset—relative to MgO(110), indicating that, at fixed hole doping, films grown on STO exhibit a smaller c-axis parameter due to tensile strain imparted by the substrate. Conversely, films deposited on MgO experience substrate-induced compressive strain; consequently, at a given oxygen doping, their c-axis parameter exceeds the bulk value. In our Zn-doped thin films grown on STO (001), a pronounced leftward and downward shift is also observed as shown in Figure 3.19c. The leftward shift—i.e., toward lower temperatures—primarily reflects a narrowing and depression of the superconducting dome in the phase diagram; consequently, at fixed hole doping level, the critical temperatures are reduced. Conversely, the downward vertical shift may be attributable attributable to the presence of zinc. It should also be noted that, due to Zn, superconductivity is lost earlier, so we have fewer samples; for this reason, in Figure 3.19c the Zn-doped YBCO curve is shorter.

At this stage, since we know the c-axis and the critical temperature for each Zn-doped YBCO sample, we use (i) the dependence c-axis(T_c), (ii) the dependence of T_c on hole doping from the phase diagram, and (iii) the relation between c-axis and hole doping for pure YBCO films; all of these are reported in paper [20]. First, we used c-axis(T_c) because—as explained in the previous paragraph and shown in Figure 3.19c—the shape of c-axis(T_c) is the same in all cases (including Zn-doped samples), differing only by rigid shifts. We therefore took an c-axis(T_c) curve from paper [20] as a reference and translated the c-axis(T_c) of our Zn-doped samples to align with it, thereby obtaining new "shifted" c-axis values and critical temperatures T_c that can then serve as inputs to infer the hole-doping level via the relations measured for pure YBCO in Reference [20], as the phase diagram and the plot of c-axis versus hole doping level.

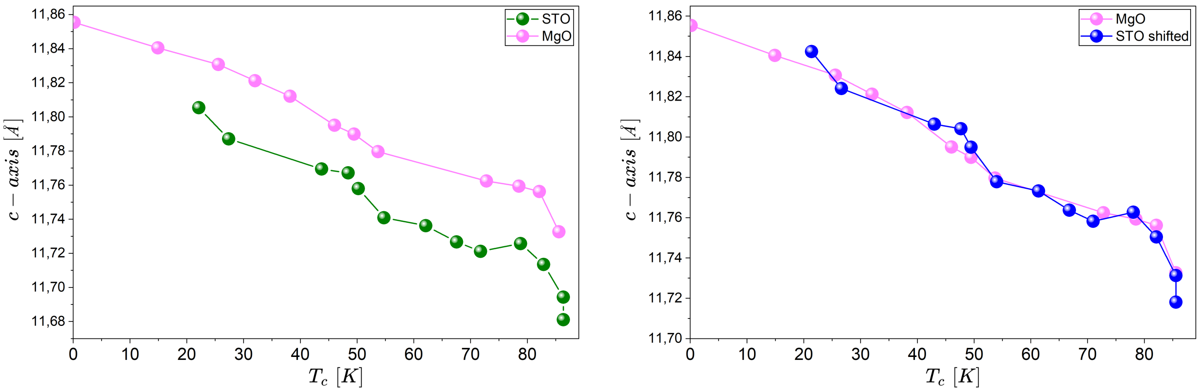

(a) Samples of YBCO deposited on (110) MgO substrates and on (001) STO substrates. Data taken from [20]

(b) Samples of YBCO deposited on (110) MgO substrates and on (001) STO substrates shifted relative to MgO

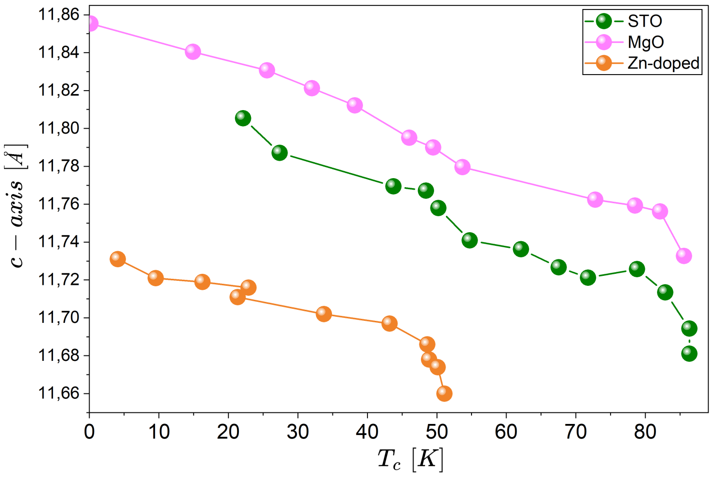

(c) Samples of Zn-doped YBCO deposited on (001) STO

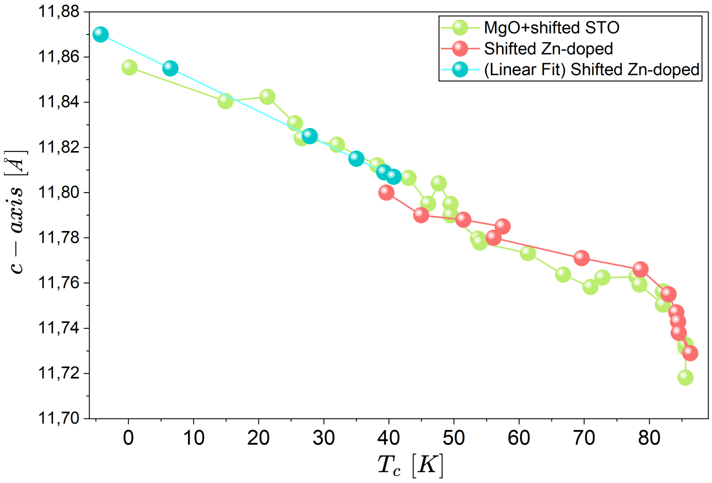

(d) Samples of Zn-doped YBCO deposited on (001) STO shifted toward the curve MgO$^+$STO, and the linearized values of T_c

Figure 3.19: c-axis parameter versus critical temperature for the various samples

To increase data coverage, we have constructed a single master curve. We have chosen the YBCO films on MgO(110) as the reference dataset (as it is the most complete) and rigidly shifted the YBCO data grown on STO (001) so that they collapse onto the MgO(110) dataset, yielding the unified curve shown in Figure 3.19b.

Once the new reference curve (shown in green in Figure 3.19d) is established, we shift the data of the Zn-doped samples relative to this reference curve, obtaining new c-axis values and critical temperatures. The Zn-doped curve shown in red in Figure 3.19d corresponds to specimens for which both the c-axis and a critical temperature are available; however, as noted, many Zn-doped samples do not exhibit a measurable critical temperature because the superconducting phase is strongly suppressed in these films. To understand how to assign new critical temperatures to our Zn-doped YBCO samples—which do not exhibit a superconducting transition but for which we have c-axis measurements—we need to pause briefly to consider the behavior of the c-axis(T_c) curve. By examining the master curve we constructed—or simply the one for YBCO deposited on MgO(110) as shown in Figure 3.19c—one can see that, at low critical temperatures, the behavior is approximately linear. Accordingly, we performed a linear fit to the low-temperature portion of our master curve (which contains more data), thereby obtaining the slope and intercept of the linear equation that fits this temperature range. This linear-fit equation can be used to derive new critical temperatures associated with measured c-axis values; thus, for Zn-doped samples that lack a measured critical temperature but for which the c-axis was measured, we can assign a critical temperature that lies on the master curve (i.e., the one we created by merging the pure YBCO data on MgO and STO), as shown in Figure 3.19d where the new data for the Zn-doped samples are marked in turquoise. In this way, we obtained shifted c-axis and T_c values that can be used as inputs to the phase diagram $T_c(p)$ and to the $p(c\text{-axis})$ relation to determine the hole-doping levels of our samples. It should be noted, however, that the newly assigned critical temperature for CALAS_13 on the new master curve is negative (the first point of the turquoise curve shown in Figure 3.19d). Consequently, a specific methodology must be adopted to resolve this issue.

In the next step we adopted the following methodology to determine the hole-doping level. First, we assume that, although in our Zn-doped YBCO the critical temperatures (and consequently the superconducting dome) are reduced, the dome nevertheless retains the same shape as in pure YBCO. We then use the phase diagram reported in paper [20] and plotted in Figure 3.20, which relates the critical temperature to the hole-doping level via the superconducting dome for pure YBCO grown on MgO (110). By locating our critical temperatures on that dome, we assigned the corresponding hole-doping levels read from Figure 3.20. At this point, it is straightforward to conclude that for sample CALAS_13, which yields a negative temperature on the master curve, the hole-doping level cannot be inferred with this method. We also encounter another issue: near optimal doping and beyond (i.e., in the over-doped samples), points on the superconducting dome show large variations in hole doping for very small changes in the critical temperature, and the annealing 14,15,16, 17 and CALAS_26 have very similar critical temperatures, making the method unreliable for these samples. Consequently, an alternative approach must be used for these cases. Below, in Table 3.6, we list the samples to which this method was applied.

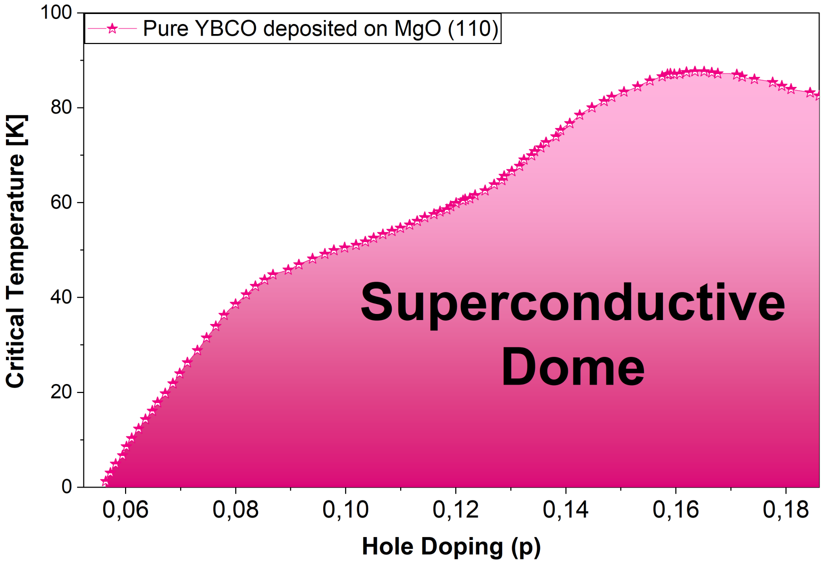

Figure 3.20: Superconductive Dome of Pure YBCO deposited on MgO(001). Data taken from [20]

To develop an alternative method for determining the hole-doping level of the remaining samples, we focus on the plot showing the dependence of the hole-doping level (p) on the c-axis for pure YBCO grown on MgO(110), shown in Figure 3.21 and taken from [20]. There, one can see that for $p > 0.14$ and for $p < 0.06$ (precisely the range for which we still need to assign a hole-doping level), the curve can be linearized. In this way, we bypass the issue of the negative critical temperature of CALAS_13, because we can use its shifted c-axis—obtained from the master curve—as the input to determine its hole-doping level using the linear fit equation of the plot shown in Figure 3.21 for $p < 0.06$.

Subsequently, to determine the hole-doping level of samples with very similar critical temperatures, one could repeat the previous procedure—i.e., linearize the p(c-axis) curve for p>0.14—but we opted for a related alternative approach. In particular, we exploit the fact that samples deposited and subsequently cooled in situ at 5°/min under 900 $mbar$

promote full oxidation of the YBCO chains, thereby yielding slightly over-doped films [20]. In our case, the thin film CALAS_26 was essentially grown under these conditions; we therefore assume that CALAS_26 corresponds to our slightly over-doped sample and assign p=0.19 to it. Using the phase diagram in Figure 3.20 we had determined hole-doping levels up to p=0.143, as mentioned on Table 3.6; inspection of Figure 3.21 (p vs c-axis) shows that beyond this value the behavior is linear. Assuming that this linearity also holds for Zn-doped YBCO (as suggested, for samples with $p>0.143$, by the trend of c-axis versus post-annealing pressure in Figure 3.18), we performed a linearization from p=0.143 (from the phase diagram) to p=0.19 (CALAS_26). The resulting linear relation was then used to estimate the hole-doping levels for samples in the range $0.143<p<0.19$, as reported in Table 3.6.

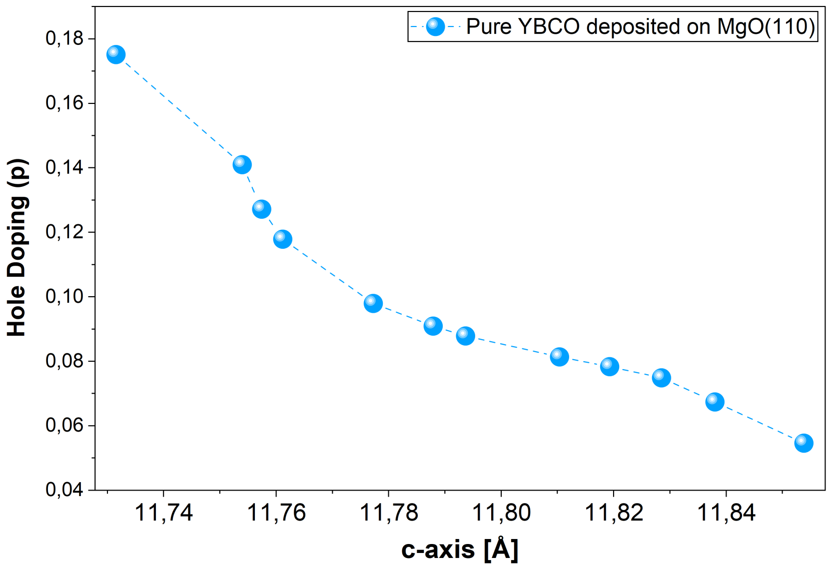

Figure 3.21: Hole doping versus the c-axis parameter of pure YBCO deposited on MgO (110). Data taken from [20].

CALAS	P_{ann} [mbar]	p (Hole Doping)	Methodology for determining the hole-doping level
30_13	6.00E-05	0.042	Linearization of p(c-axis) for p<0.06 in Figure 3.21.
30_12	1.50E-04	0.060	Determination using the phase diagram in Figure 3.20.
30_11	4.00E-04	0.072	Determination using the phase diagram in Figure 3.20.
30_10	6.60E-04	0.077	Determination using the phase diagram in Figure 3.20.
30_9	9.30E-04	0.081	Determination using the phase diagram in Figure 3.20.
30_8	2.00E-03	0.083	Determination using the phase diagram in Figure 3.20.
30_2	4.00E-03	0.082	Determination using the phase diagram in Figure 3.20.
30_7	5.00E-03	0.088	Determination using the phase diagram in Figure 3.20.
30_6	6.00E-03	0.103	Determination using the phase diagram in Figure 3.20.
30_3	8.00E-03	0.116	Determination using the phase diagram in Figure 3.20.
30_4	1.30E-02	0.114	Determination using the phase diagram in Figure 3.20.
30_5	3.00E-02	0.133	Determination using the phase diagram in Figure 3.20.
30_1	1.00E-01	0.143	Determination using the phase diagram in Figure 3.20.
30_14	7.90E+00	0.158	Determination via linearization using p=0.19 and p=0.143 as reference points.
30_15	7.50E+01	0.168	Determination via linearization using p=0.19 and p=0.143 as reference points.
30_16	3.60E+02	0.173	Determination via linearization using p=0.19 and p=0.143 as reference points.
26	7.20E+02	0.190	Determination via linearization using p=0.19 and p=0.143 as reference points.
30_17	8.40E+02	0.179	Determination via linearization using p=0.19 and p=0.143 as reference points.

Table 3.6: Hole-doping level determination for the CALAS series.

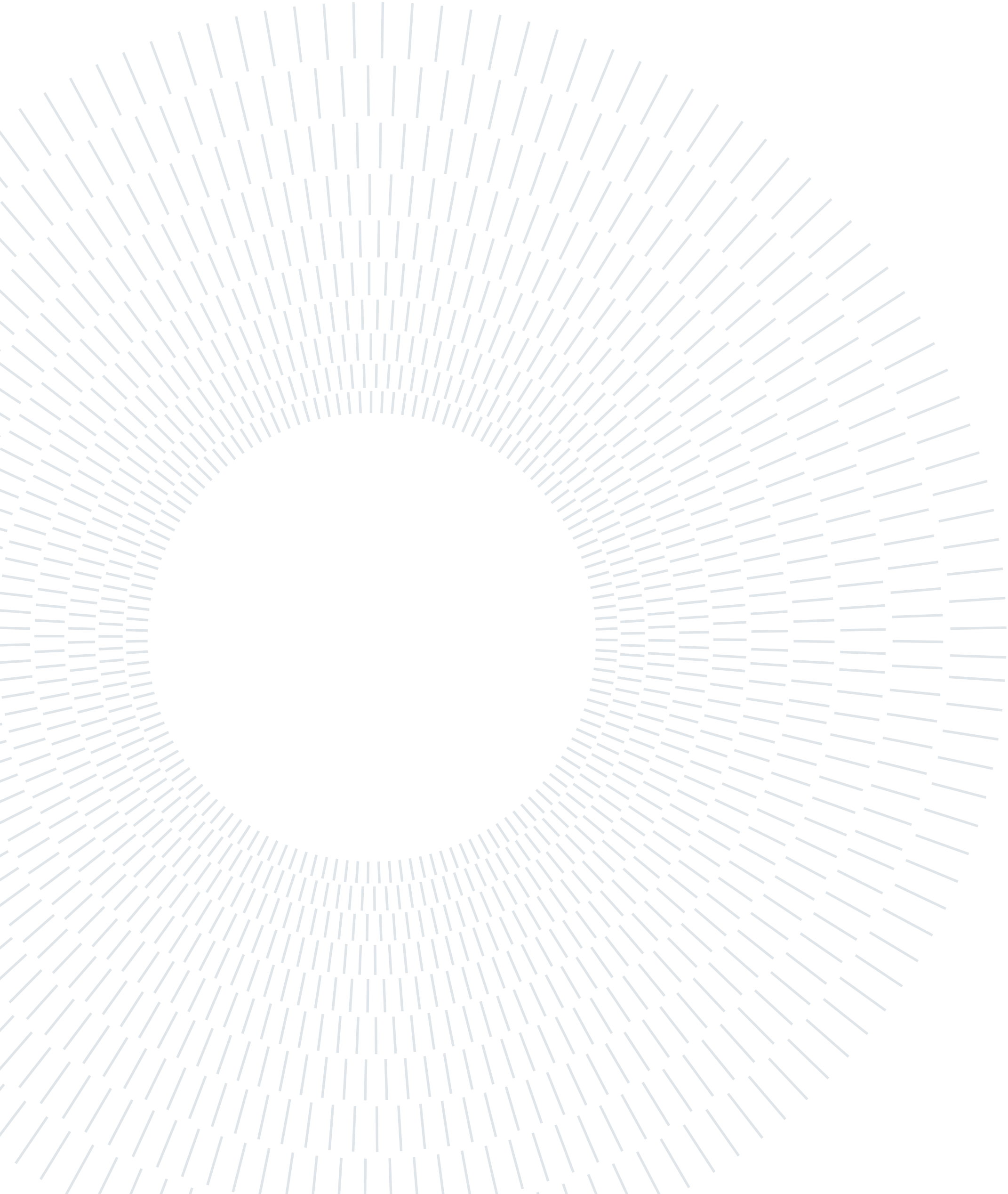

4 | Phase Diagram

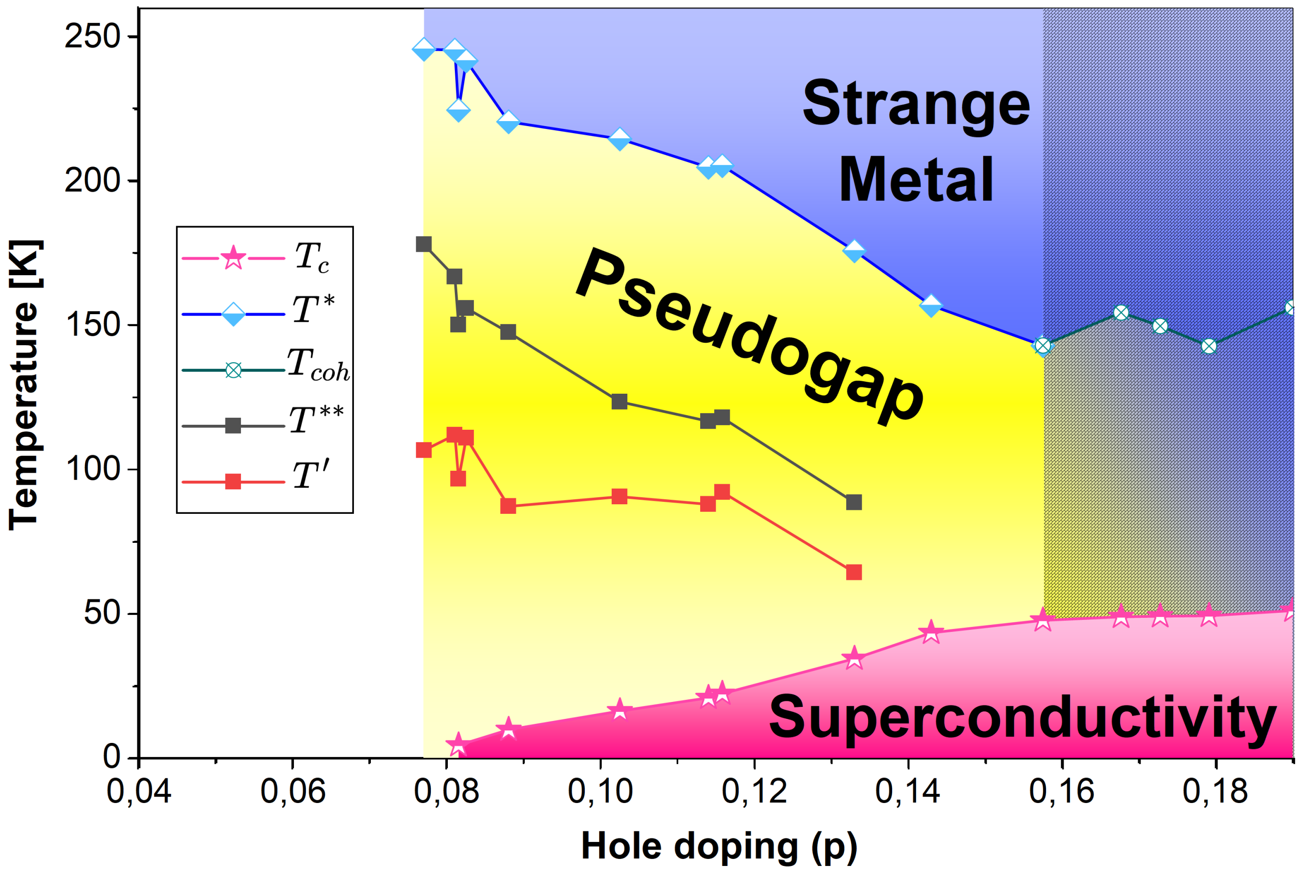

Figure 4.1: Phase Diagram of Zn-doped YBCO thin film

Finally, in this chapter we compiled all characteristic temperatures extracted from transport measurements and mapped them to the corresponding hole-doping levels determined in the previous chapter, in order to construct the phase diagram of the Zn-doped YBCO thin film (thickness $\approx 60\,nm$), shown in Fig. 4.1 .

In our phase diagram, four color-coded regions can be identified: (i) yellow, denoting the Pseudogap, lying between the pseudogap temperatures T^* and the critical temperatures

T_c; (ii) magenta, representing the superconducting phase, below T_c; (iii) blue, associated with the Strange Metal, above T^*; and (iv) the shaded region, corresponding to over-doped samples. As discussed in Section 3.2, in this latter regime the parabolic contribution of the CuO chains to the temperature-dependent resistance obscures the true T^*, allowing only the T_{coh} to be identified. Consequently, the boundary between the Pseudogap and the Strange Metal cannot be delineated sharply.

From top to bottom, the first characteristic temperature is the pseudogap temperature. Although it cannot be determined across the full hole-doping range, the available underdoped data, T^* decreases with increasing hole doping, as expected; however, around $0.11 < p < 0.13$ the slope of T^* changes and becomes steeper (i.e., more negative). The next scale is T^{**}, associated with the upper bound of the quadratic-in-temperature resistivity regime; below it we identify T', the lower bound of that quadratic regime; and, finally, the critical temperature, which delineates the superconductive dome. As noted previously when discussing the pure YBCO phase diagram (Section 1.5), the slightly overdoped sample does not typically coincide with the maximum critical temperature; unexpectedly, in our case the slightly overdoped specimen at $p = 0.19$ attains the highest critical temperature within our superconductive dome, indicating a shift in the dome's position relative to pure YBCO. To better contextualize these results, we compare our Zn-doped YBCO thin film grown on STO (001) with a reference pure YBCO film on the same substrate; accordingly, Figure 4.2 contrasts the phase diagrams of the Zn-doped and pristine systems.

In the Figure 4.2, the data for pure YBCO are shown in orange, whereas the Zn-doped samples are plotted in azure. A comparison of the pseudogap temperature versus hole-doping level reveals closely matching trends across the two datasets. Pure YBCO, however, systematically exhibits higher pseudogap temperatures at comparable doping, and the change in slope occurs at a slightly larger hole-doping level relative to the Zn-doped series, but for hole doping level $p > 0.13$, the two curves appear to converge. This observation suggests that Zn substitution exerts a negligible effect on the pseudogap temperature in the overdoped regime. Consistent with this view, literature data [50] for a single crystal sample with lower Zn content, $YBa_2(Cu_{0.95}Zn_{0.007})_3O_7$, indicate that the pseudogap temperatures T^* remain unchanged upon Zn doping. Hence, the slight variations observed in the pseudogap temperature may be attributable to extrinsic factors rather than Zn substitution. In any case, within the hole-doping range relevant to the study of CDF's, the two series appear to converge, reproducing the same effect reported in paper [50]. However, any such conclusion requires future direct determination of the overdoped pseudogap temperatures.

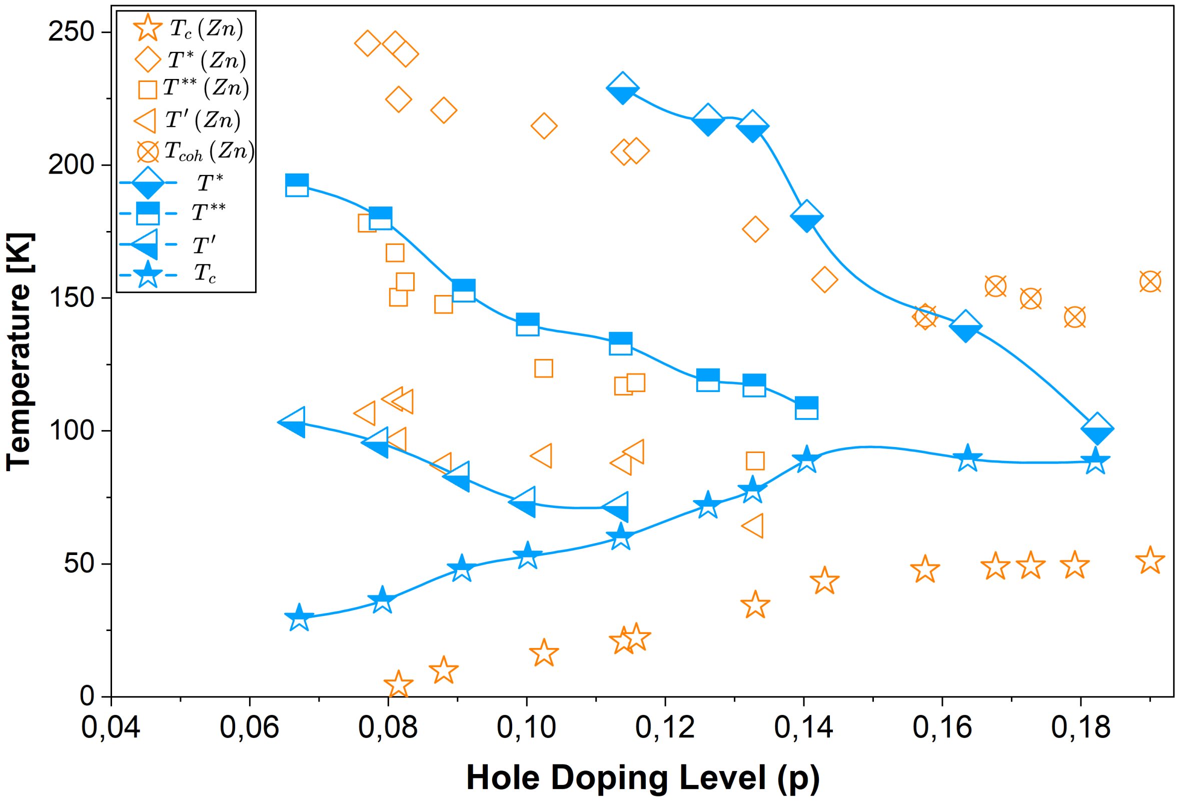

Figure 4.2: Phase diagram of Zn-doped YBCO (orange) and pure YBCO (light blue), both deposited on STO (001). Data taken from [20]

The T^{**} values of Zn-doped YBCO thin films and pure YBCO exhibit the same trend for $p < 0.9$, with very similar temperatures. For $p > 0.9$, however, the T^{**} values of the Zn-doped samples fall below those of pure YBCO. In addition, for pure YBCO the series appears to touch the superconductive dome near $p \approx 0.15$; although T^{**} is not available at that hole-doping level for Zn-doped YBCO samples, the comparison at $p \approx 0.13$ shows a substantially lower value in the Zn-doped samples than in pure YBCO, consistent with our superconductive dome shifted to lower temperatures in the Zn-doped samples.

The T' temperatures of the Zn-doped samples exhibit a trend less similar to that of pure YBCO and are slightly higher. This indicates that the region where a $\propto R^2$ behavior is observed is modestly reduced in the Zn-doped samples relative to pure YBCO. Near $p \approx 0.12$, in pure YBCO the T' series appears to approach the superconductive dome, whereas in the Zn-doped samples—since the superconductive dome lies at lower temperatures—the T' series decreases more sharply toward the dome.

Finally, we consider the critical temperatures T_c. As previously discussed, in the Zn-doped samples the T_c values are systematically lower, consistent with the Zn-induced suppression of superconductivity. As hypothesized, the superconductive dome retains a shape similar to that of pure YBCO, yet exhibits meaningful differences. Specifically, the maximum critical temperature occurs at $p = 0.19$ for Zn-doped YBCO, whereas for pure YBCO it is expected within $0.14 < p < 0.16$. This suggests not only a downward shift of the superconductive dome, but also a possible rightward displacement along the p axis. In paper [51], single-phase polycrystalline samples of $Y_{1-x}Ca_xBa_2(Cu_{1-y}Zn_y)_3O_{7-\delta}$ were analyzed. The incorporation of Ca, which introduces hole carriers in the CuO2 planes independently of the oxygenation state of the $CuO_{1-\delta}$ chains, enabled controlled access to the overdoped regime up to $p > 0.18$. In the overdoped samples, an asymmetric narrowing of the superconducting dome is observed: the optimal doping level (i.e., the doping that yields the maximum critical temperature) shifts to higher hole concentrations as the Zn content increases. Consequently, the rightward shift of our superconducting dome observed in our data is consistent with the literature.

5 | Conclusion

The goals of this thesis were twofold: (i) to optimize the Pulsed Laser Deposition (PLD) growth of $YBa_2[Cu_{0.95}Zn_{0.05}]_3O_{7-\delta}$ (Zn-YBCO) thin films and (ii) to construct, from transport and X-ray diffraction (XRD) measurements, a phase diagram assessing to what extent the Zn-doped sample preserves the properties of pristine YBCO—apart from the targeted suppression of superconductivity, which enables access to other state regions otherwise screened.

Concerning deposition, films on STO (001) were grown using parameters rather close to those previously employed for high-quality pristine YBCO on STO (001) at the Department of Microtechnology and Nanoscience at the Chalmers University of Technology. These conditions proved effective for Zn-YBCO as well, indicating that, at the present doping level, Zn does not appreciably alter the plasma plume dynamics, stoichiometric transfer to the substrate, or surface kinetics. To further substantiate that Zn does not degrade film quality under YBCO-like growth conditions, morphological characterization by scanning electron microscopy (SEM) and atomic force microscopy (AFM) would be valuable. These measurements were not performed during the stay at Chalmers due to instrument maintenance and limited training time.

XRD (symmetric $2\theta - \omega$ scans) confirms that the films are crystalline and c-axis oriented, exhibiting the expected increase of the 2θ angle of $(00l)$ peaks with increasing hole doping. In Zn-doped samples, the peaks are slightly shifted to higher angles relative to pristine YBCO; therefore smaller c-axis values were found in our Zn-YBCO samples; however, moving toward the overdoped regime the values become closer (in the slightly overdoped case, the c-axis is $\approx 11.66,$ for Zn-YBCO and $\approx 11.68,$ for the pure sample). According to the literature [32], the introduction of zinc does not modify the lattice parameters of polyceramic YBCO samples; note also that our specimens are thin films and that the c-axis comparison was performed between films with different thickness (ours $\approx 60, nm$, the comparison films $\approx 30, nm$). For underdoped samples, the presence of Silver in the silver paste and Gold in the contact pads used for transport measurements partially obscured some reflections, reducing the number of peaks usable for accurate c-axis determination.

Transport measurements (PPMS) reveal, in samples near the overdoped regime, an upward parabolic contribution in $R(T)$ attributable to CuO chains (also observed in pristine YBCO), which tends to mask the true T^*. A viable route forward is to detwin the film by selecting an alternative substrate so that resistivity can be measured along the a-axis, thus removing the contribution of chains along b. In the underdoped samples—where the T_{linear} should approximate T^*—we observe slightly reduced T^* values compared to pristine YBCO. This trend is not fully consistent with prior reports stating that Zn does not affect T^*—supporting a pseudogap competing with, yet distinct from, superconductivity—and may therefore reflect extrinsic factors. Although pristine-YBCO data near $p > 0.14$ are limited, the two series appear to converge; moreover, T^* values at the lowest hole dopings are unavailable for pristine YBCO. An expanded dataset is thus required.

As expected, Zn suppresses the critical temperatures; in addition, our films display a shift of the optimal doping toward $p \approx 0.19$, together with a narrowing and rightward shift of the superconducting dome. If the maximum T_c indeed occurs at $p = 0.19$, it would coincide with the putative quantum critical point (QCP) associated with the strange-metal phase, hinting at further interconnections among these orders. One possible explanation for the shift in doping of the maximum critical temperature could be related to the CDW order, which is known to compete with superconductivity and may be modified in Zn-doped samples. Indeed, pioneering spectroscopic measurements have suggested that CDW order is weaker in Zn-substituted cuprates [52]. If this scenario were confirmed, a reduced CDW strength would imply a weaker competition with superconductivity, leading to an enhancement of Tc and thus shifting its maximum towards $p \approx 0.19$. To fully clarify this scenario, further spectroscopic investigations are required - for instance, RIXS experiments on Zn-doped samples across different oxygen doping levels. This is precisely the direction I followed in this thesis, where the successful growth of such samples has laid the groundwork for future studies.

In order to obtain an even clearer picture of how Zn affects the superconducting and normal-state properties of YBCO, a deeper exploration of the overdoped regime is required, by further increasing the hole doping.; to achieve this, one may substitute Y^{3+} ions with Ca^{2+}, which introduces additional hole-type carriers in the CuO planes in a (quasi) oxygenation-independent manner with respect to the chains, thereby enabling robust access to the overdoped regime $p > 0.19$.

In summary, although superconductivity is suppressed as expected, many fundamental properties of Zn-YBCO remain similar to pristine YBCO (with largely unchanged lattice parameters and only modest differences in T^*). By characterizing Zn-YBCO thin films across different hole-doping levels, this work establishes a new material platform for future investigations. On one hand, it enables RIXS studies of collective density fluctuations within the superconducting dome, free from the masking effect of superconductivity, thereby providing a direct test of the possible existence of a hidden quantum critical point. On the other hand, it opens the way to explore other regions of the phase diagram and to clarify how Zn substitution modifies charge, magnetic, lattice, and orbital excitations.

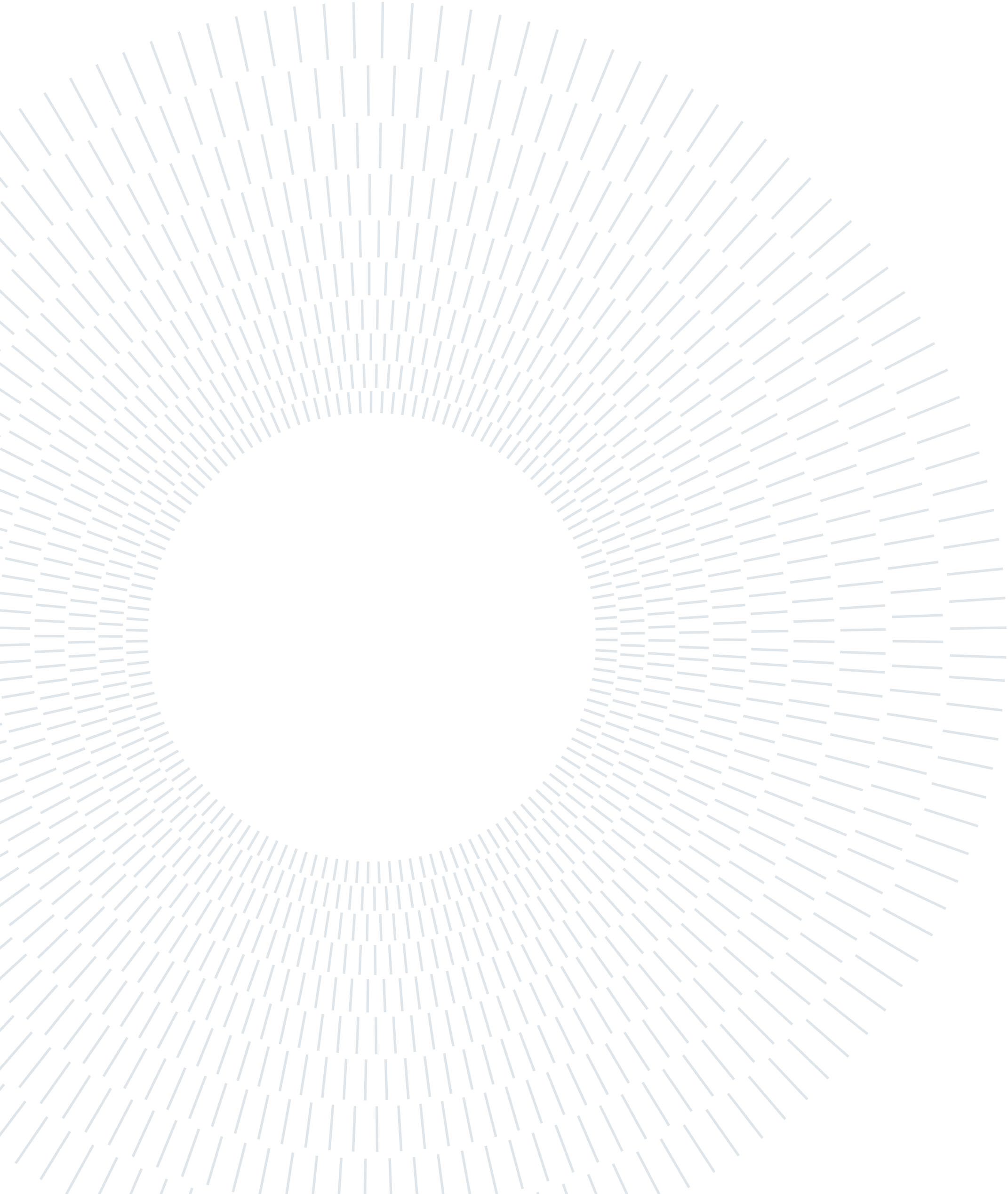

Bibliography

[1] W. Meissner and R. Ochsenfeld. ”Ein neuer effekt bei eintritt der supraleitfähigkeit”. *Naturwissenschaften*, 21(44):787–788, 1933.

[2] F. London, H. London, and Frederick Alexander Lindemann. ”The electromagnetic equations of the supraconductor”. *Proceedings of the Royal Society of London. Series A - Mathematical and Physical Sciences*, 149(866):71–88, 1935.

[3] L. D. Landau. On the theory of phase transitions. *Zh. Eksp. Teor. Fiz.*, 7:19–32, 1937.

[4] V. L. Ginzburg. On the theory of superconductivity. *Il Nuovo Cimento (1955-1965)*, 2(6):1234–1250, 1955.

[5] Emanuel Maxwell. Isotope effect in the superconductivity of mercury. *Phys. Rev.*, 78:477–477, 1950.

[6] J. Bardeen, L. N. Cooper, and J. R. Schrieffer. Theory of superconductivity. *Phys. Rev.*, 108:1175–1204, 1957.

[7] Harald Ibach and Hans Lüth. *Solid-State Physics: An Introduction to the Theory*. Springer, Berlin, 2nd edition, 2003.

[8] W. L. McMillan. Transition temperature of strong-coupled superconductors. *Phys. Rev.*, 167:331–344, 1968.

[9] J. G. Bednorz and K. A. Müller. Possible hightc superconductivity in the balacuo system. *Zeitschrift für Physik B Condensed Matter*, 64(2):189–193, 1986.

[10] M. K. Wu, J. R. Ashburn, C. J. Torng, P. H. Hor, R. L. Meng, L. Gao, Z. J. Huang, Y. Q. Wang, and C. W. Chu. Superconductivity at 93 k in a new mixed-phase y-ba-cu-o compound system at ambient pressure. *Phys. Rev. Lett.*, 58:908–910, 1987.

[11] Defang Duan, Hongyu Yu, Hui Xie, and Tian Cui. Ab initio approach and its impact on superconductivity. *Journal of Superconductivity and Novel Magnetism*, 32(1):53–60, 2019.

[12] Muhammad Talha Masood. *Solution-Processable Compact and Mesoporous Titanium Dioxide Thin Films as Electron-Selective Layers for Perovskite Solar Cells.* PhD thesis, 2020.

[13] B. Keimer, S. A. Kivelson, M. R. Norman, S. Uchida, and J. Zaanen. From quantum matter to high-temperature superconductivity in copper oxides. *Nature*, 518(7538):179–186, 2015.

[14] S. D. Brorson, R. Buhleier, I. E. Trofimov, J. O. White, Ch. Ludwig, F. F. Balakirev, H.-U. Habermeier, and J. Kuhl. Electrodynamics of high-temperature superconductors investigated with coherent terahertz pulse spectroscopy. *J. Opt. Soc. Am. B*, 13(9):1979–1993, 1996.

[15] R. A. Cooper, Y. Wang, B. Vignolle, O. J. Lipscombe, S. M. Hayden, Y. Tanabe, T. Adachi, Y. Koike, M. Nohara, H. Takagi, C. Proust, and N. E. Hussey. Anomalous criticality in the electrical resistivity of $\mathrm{La}_{2-x}\mathrm{Sr}_x\mathrm{CuO}_4$. *Science*, 323(5914):603–607, 2009.

[16] C. M. Varma. Non-fermi-liquid states and pairing instability of a general model of copper oxide metals. *Phys. Rev. B*, 55:14554–14580, 1997.

[17] Subir Sachdev. Where is the quantum critical point in the cuprate superconductors? *physica status solidi (b)*, 247(3):537–543, 2010.

[18] Götz Seibold, Riccardo Arpaia, Ying Ying Peng, Roberto Fumagalli, Lucio Braicovich, Carlo Di Castro, Marco Grilli, Giacomo Claudio Ghiringhelli, and Sergio Caprara. Strange metal behaviour from charge density fluctuations in cuprates. *Communications Physics*, 4(1):7, 2021.

[19] Marco Grilli, Carlo Di Castro, Giovanni Mirarchi, Götz Seibold, and Sergio Caprara. Dissipative quantum criticality as a source of strange metal behavior. *Symmetry*, 15(3), 2023.

[20] Riccardo Arpaia, Eric Andersson, Edoardo Trabaldo, Thilo Bauch, and Floriana Lombardi. Probing the phase diagram of cuprates with $\mathrm{YBa}_2\mathrm{Cu}_3\mathrm{O}_{7-\delta}$ thin films and nanowires. *Phys. Rev. Mater.*, 2:024804, 2018.

[21] R. Arpaia, S. Caprara, R. Fumagalli, G. De Vecchi, Y. Y. Peng, E. Andersson, D. Betto, G. M. De Luca, N. B. Brookes, F. Lombardi, M. Salluzzo, L. Braicovich, C. Di Castro, M. Grilli, and G. Ghiringhelli. Dynamical charge density fluctuations pervading the phase diagram of a Cu-based high-T_c superconductor. *Science*, 365(6456):906–910, 2019.

[22] Carlo Di Castro. Revival of charge density waves and charge density fluctuations in cuprate high-temperature superconductors. *Condensed Matter*, 5(4), 2020.

[23] R. W. Cahn and P. Haasen, editors. *Phase Transformations, Nondiffusive.* North-Holland, Amsterdam, 1996. Fourth Edition.

[24] Eric Wahlberg, Riccardo Arpaia, Götz Seibold, Matteo Rossi, Roberto Fumagalli, Edoardo Trabaldo, Nicholas B. Brookes, Lucio Braicovich, Sergio Caprara, Ulf Gran, Giacomo Ghiringhelli, Thilo Bauch, and Floriana Lombardi. Restored strange metal phase through suppression of charge density waves in underdoped $\mathrm{YBa}_2Cu_3O_7.Science, 373(6562):1506–1510, 2021.$

[25] J. Chang, E. Blackburn, O. Ivashko, A. T. Holmes, N. B. Christensen, M. Hücker, Ruixing Liang, D. A. Bonn, W. N. Hardy, U. Rütt, M. v. Zimmermann, E. M. Forgan, and S M Hayden. Magnetic field controlled charge density wave coupling in underdoped $\mathrm{YBa}_2Cu_3O_{6+x}.Nature\ Communications, 7(1), 2016.$

[26] Tao Wu, Hadrien Mayaffre, Steffen Krämer, Mladen Horvatić, Claude Berthier, W. N. Hardy, Ruixing Liang, D. A. Bonn, and Marc-Henri Julien. Magnetic-field-induced charge-stripe order in the high-temperature superconductor $\mathrm{YBa}_2Cu_3O_y.Nature, 477(7363):191–194, 2011.$

[27] Riccardo Arpaia and Giacomo Ghiringhelli. Charge order at high temperature in cuprate superconductors. *Journal of the Physical Society of Japan*, 90(11):111005, 2021.

[28] Riccardo Arpaia, Leonardo Martinelli, Marco Moretti Sala, Sergio Caprara, Abhishek Nag, Nicholas B. Brookes, Pietro Camisa, Qizhi Li, Qiang Gao, Xingjiang Zhou, Mirian Garcia-Fernandez, Ke-Jin Zhou, Enrico Schierle, Thilo Bauch, Ying Ying Peng, Carlo Di Castro, Marco Grilli, Floriana Lombardi, Lucio Braicovich, and Giacomo Ghiringhelli. Signature of quantum criticality in cuprates by charge density fluctuations. *Nature Communications*, 14(1):7198, 2023.

[29] S. Uchida. Zn-impurity effects on high-temperature superconductivity. *Physica C: Superconductivity*, 357-360:25–29, 2001.

[30] Rishi Kumar Singhal. How the substitution of Zn for Cu destroys superconductivity in YBCO system? *Journal of Alloys and Compounds*, 495(1):1–6, 2010.

[31] Gang Xiao, M. Z. Cieplak, D. Musser, A. Gavrin, F. H. Streitz, C. L. Chien, J. J. Rhyne, and J. A. Gotaas. Significance of plane versus chain sites in high-temperature oxide superconductors. *Nature*, 332(6161):238–240, 1988.

[32] S. Zagoulaev, P. Monod, and J. Jégoudez. Magnetic and transport properties of Zn-doped $YBa_2Cu_3O_7$ in the normal state. *Phys. Rev. B*, 52:10474–10487, 1995.

[33] Matthieu Le Tacon, A. Sacuto, Y. Gallais, E. Sherman, A. Forget, and D. Colson. Effects of magnetic and non-magnetic impurities on the superconducting state of $YBa_2Cu_3O_{7-\delta}$. 2005.

[34] Henri Alloul. What do we learn from impurities and disorder in high-Tc cuprates? *Frontiers in Physics*, 12:1406242, 2024.

[35] D. J. C. Walker, A. P. Mackenzie, and J. R. Cooper. Transport properties of Zinc-doped $YBa_2Cu_3O_{7-\delta}$ thin films. *Phys. Rev. B*, 51:15653–15656, 1995.

[36] Joy Mittra, Geogy Abraham, Manoj Kesaria, Sumit Bahl, Raman Singh, Sonnada Shivaprasad, Chebolu Viswanadham, Ulhas Kulkarni, and G. Dey. Role of substrate temperature in the pulsed laser deposition of zirconium oxide thin film. *Materials Science Forum*, 710:757–761, 2012.

[37] S. C. Singh, C. Fallon, P. Yeates, C. McLoughlin, and J. T. Costello. Spot size dependent shock wave, plume and ion expansion dynamics of laser produced ybco plasma, 2024.

[38] Joachim Maier. *Physical Chemistry of Ionic Materials: Ions and Electrons in Solids.* John Wiley & Sons Ltd, Chichester, UK, 2004.

[39] Riccardo Arpaia, Eric Andersson, Alexei Kalaboukhov, Elsebeth Schröder, Edoardo Trabaldo, Regina Ciancio, Goran Dražić, Pasquale Orgiani, Thilo Bauch, and Floriana Lombardi. Untwinned $YBa_2Cu_3O_{7-\delta}$ thin films on MgO substrates: A platform to study strain effects on the local orders in cuprates. *Phys. Rev. Mater.*, 3:114804, 2019.

[40] Riccardo Arpaia, Núria Alcalde-Herraiz, Andrea D'Alessio, Evgeny Stepantsov, Eric Wahlberg, Alexei Kalaboukhov, Thilo Bauch, and Floriana Lombardi. Engineering underdoped CuO_2 nanoribbons in nm-thick a-axis $YBa_2Cu_3O_{7-\delta}$ films. *Phys. Rev. Mater.*, 8:044803, 2024.

[41] Eric Wahlberg. *Reshaping the phase diagram of $YBa_2Cu_3O_{7-\delta}$ through strain in ultrathin films and nanowires.* PhD thesis, Chalmers University of Technology, Gothenburg, Sweden, 2021.

[42] Riccardo Arpaia, Dmitri Golubev, Reza Baghdadi, Regina Ciancio, Goran Dražić, Pasquale Orgiani, Domenico Montemurro, Thilo Bauch, and Floriana Lombardi.

Transport properties of ultrathin $YBa_2Cu_3O_{7-\delta}$ nanowires: A route to single-photon detection. *Phys. Rev. B*, 96:064525, 2017.

[43] S. Zagoulaev, P. Monod, and J. Jégoudez. Magnetic and transport properties of Zn-doped $YBa_2Cu_3O_7$ in the normal state. *Phys. Rev. B*, 52:10474–10487, 1995.

[44] Eric Andersson, Riccardo Arpaia, Edoardo Trabaldo, Thilo Bauch, and Floriana Lombardi. Fabrication and electrical transport characterization of high quality underdoped $YBa_2Cu_3O_{7-\delta}$ nanowires. *Superconductor Science and Technology*, 33(6):064002, 2020.

[45] Eric Wahlberg, Riccardo Arpaia, Alexei Kalaboukhov, Thilo Bauch, and Floriana Lombardi. Doping dependence of the upper critical field in untwinned $YBa_2Cu_3O_7$ thin films. *Superconductor Science and Technology*, 36(2):024001, 2022.

[46] Eric Wahlberg, Riccardo Arpaia, Debmalya Chakraborty, Alexei Kalaboukhov, David Vignolles, Cyril Proust, Annica M. Black-Schaffer, Götz Seibold, Thilo Bauch, and Floriana Lombardi. Boosting superconductivity: how nanofaceted surfaces transform the ground state of ultrathin $YBa_2Cu_3O_{7-\delta}$ thin films, arxiv:2502.03986, (2025).

[47] Karthik Loganathan, Gaurav Kumar, Vishnu Kirthi Arivarasan, Abdul Rahuman, and Bhaskar Rao. Streptomyces sp. lk3 mediated synthesis of silver nanoparticles and its biomedical application. *Bioprocess and biosystems engineering*, 37, 2013.

[48] Riccardo Arpaia. *YBCO nanowires to study nanoscale ordering in High-T_c Superconductors*. PhD thesis, Chalmers University of Technology, Department of Microtechnology and Nanoscience (MC2), Gothenburg, Sweden, 2016. Doctoral thesis.

[49] Ruixing Liang, D. A. Bonn, and W. N. Hardy. Evaluation of CuO_2 plane hole doping in $YBa_2Cu_3O_{6+x}$ single crystals. *Phys. Rev. B*, 73(18):180505, 2006.

[50] Ece Uykur, Kiyohisa Tanaka, Takahiko Masui, Shigeki Miyasaka, and Setsuko Tajima. Persistence of the superconducting condensate far above the critical temperature of $YBa_2(Cu,Zn)_3O_y$ revealed by c-axis optical conductivity measurements for several zn concentrations and carrier doping levels. *Phys. Rev. Lett.*, 112:127003, 2014.

[51] S. H. Naqib. Effect of Zn substitution on the suppression of T_c of $Y_{1-x}Ca_xBa_2(Cu_{1-y}Zn_y)_3O_{7-\delta}$ superconductors: pseudogap and the systematic shift of the optimum hole content. *Superconductor Science and Technology*, 20(10):964–968, 2007.

[52] S Blanco-Canosa, A Frano, T Loew, Y Lu, J Porras, G Ghiringhelli, Matteo Mi-

nola, C Mazzoli, Lucio Braicovich, E Schierle, et al. Momentum-dependent charge correlations in $YBa_2Cu_3O_{6+\delta}$ superconductors probed by resonant x-ray scattering: Evidence for three competing phases. *Physical review letters*, 110(18):187001, 2013.

List of Figures

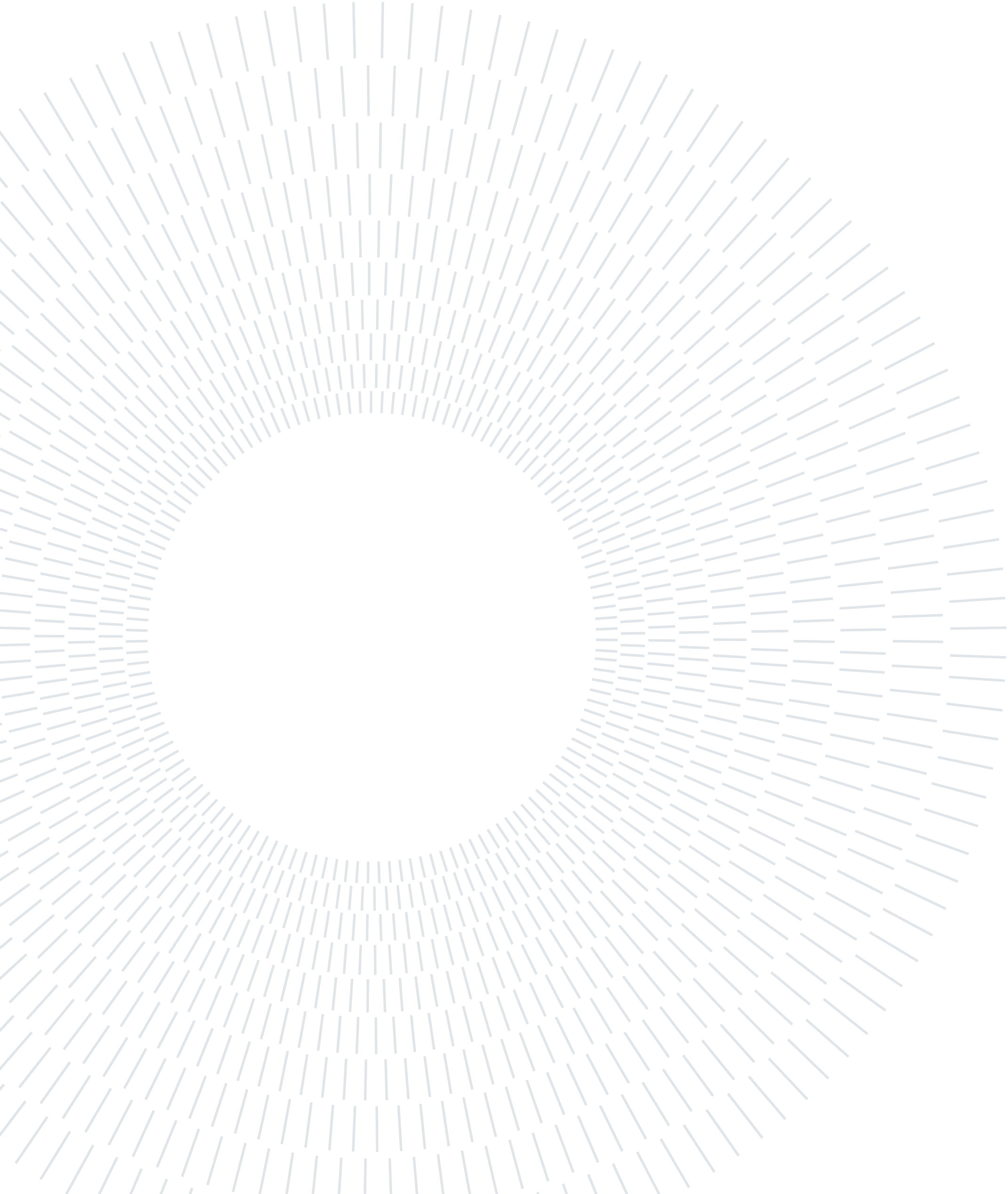

List of Tables

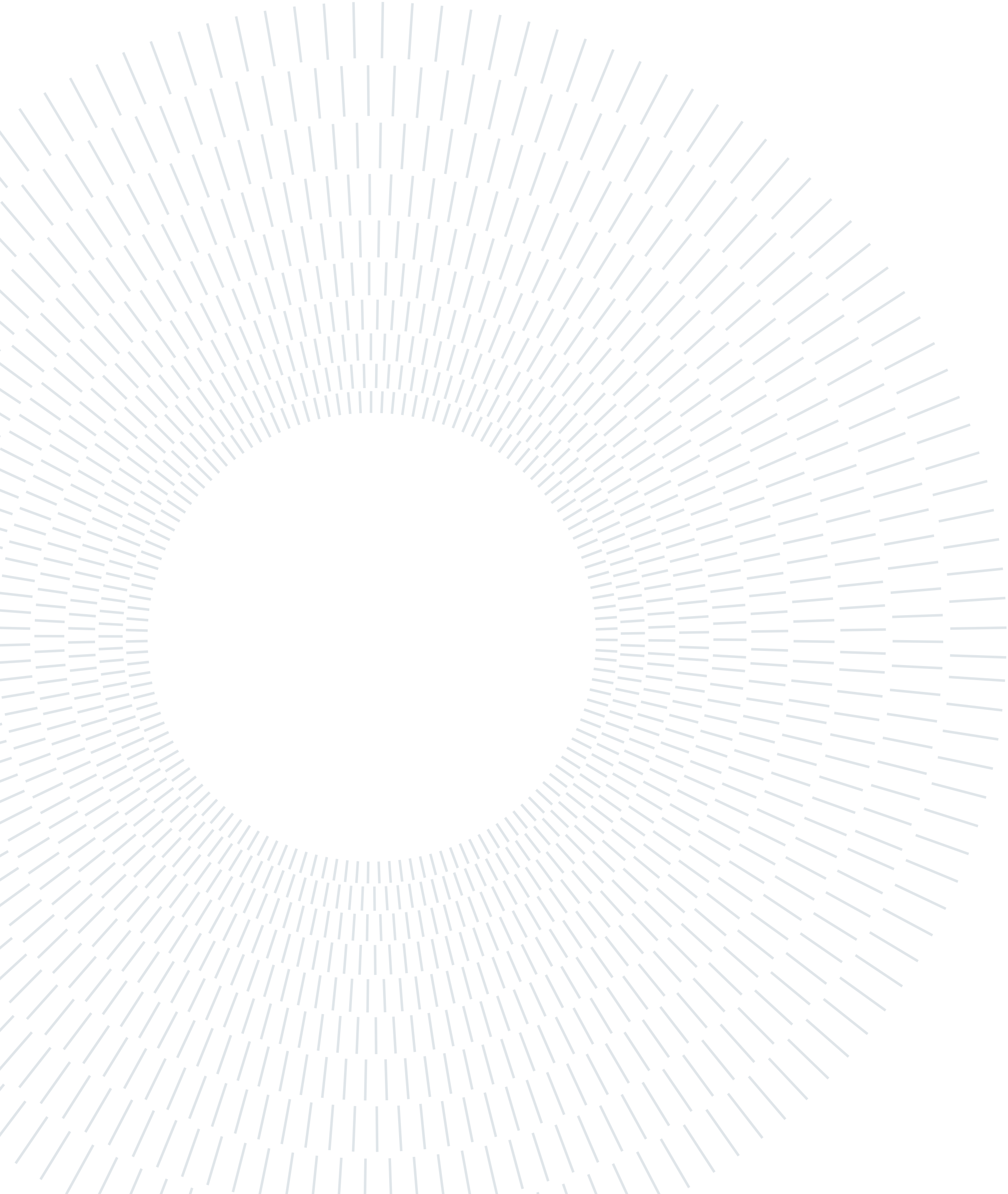

List of Abbreviations and Symbols

Abbreviation	Meaning
AFM	Atomic force microscopy
ARPES	Angle-resolved photoemission spectroscopy
CDF	Charge Density Fluctuations
CDW	Charge Density Waves
FWHM	Full width at half maximum
HTS	High-temperature superconductivity
PLD	Pulsed Laser Deposition
QCP	Quantum Critical Point
RIXS	Resonant inelastic X-ray scattering
SEM	Scanning electron microscopy
STO (001)	$SrTiO_3$ (001)-oriented
XRD	X-Ray Diffraction
YBCO	$YBa_2Cu_3O_{7-\delta}$
Zn-YBCO	$YBa_2[Cu_{0.95}Zn_{0.05}]_3O_{7-\delta}$

Symbol	Description	SI Unit
$\boldsymbol{T_c}$	Average Critical Temperature	$\boldsymbol{K}$
$\boldsymbol{T^*}$	Pseudogap Temperature	$\boldsymbol{K}$
$\boldsymbol{T_{linear}}$	Temperatura alla quale inizia il comportamento lineare	$\boldsymbol{K}$
$\boldsymbol{T_{coh}}$	"crossover temperature from a coherent and an incoherent metal state"	$\boldsymbol{K}$
$\boldsymbol{T^{**}}$	upper bound in temperature for the quadratic behaviour of $R(T)$	$\boldsymbol{K}$
$\boldsymbol{T'}$	lower bound in temperature for the quadratic behaviour of $R(T)$	$\boldsymbol{K}$
p	hole doping level	/
t	thickness of the film	$\boldsymbol{nm}$
$\boldsymbol{P_{ann}}$	Annealing Pressure	$\boldsymbol{mbar}$
$\boldsymbol{\rho_{100K}}$	Resistivity measured at 100 K	$\boldsymbol{\mu\Omega.cm}$
$\boldsymbol{H}$	Magnetic Field	$\boldsymbol{T}$